AGU PUBLICATIONS

JGR

Journal of Geophysical Research: Oceans

RESEARCH ARTICLE

10.1002/2016JC011922

Observations and modeling of a tidal inlet dye tracer plume

Falk Feddersen[1], Maitane Olabarrieta[2], R. T. Guza[1], D. Winters[3], Britt Raubenheimer[4], and Steve Elgar[4]

[1]Scripps Institution of Oceanography, La Jolla, California, USA, [2]University of Florida, Gainesville, Florida, USA, [3]Oregon State University, Corvallis, Oregon, USA, [4]Woods Hole Oceanographic Institution, Woods Hole, Massachusetts, USA

Key Points:
- A 9 km long dye plume released on ebb from a tidal inlet was observed in situ and aerial hyperspectral with dye mass balance closure
- The dye plume was well modeled with the coupled wave and circulation model COAWST
- Forcing due to breaking of obliquely incident waves have a large impact on observed and modeled dye evolution

Correspondence to:
F. Feddersen,
falk@coast.ucsd.edu

Citation:
Feddersen, F., M. Olabarrieta, R. T. Guza, D. Winters, B. Raubenheimer, and S. Elgar (2016), Observations and modeling of a tidal inlet dye tracer plume, *J. Geophys. Res. Oceans*, *121*, doi:10.1002/2016JC011922.

Received 28 APR 2016
Accepted 30 SEP 2016
Accepted article online 4 OCT 2016

Abstract A 9 km long tracer plume was created by continuously releasing Rhodamine WT dye for 2.2 h during ebb tide within the southern edge of the main tidal channel at New River Inlet, NC on 7 May 2012, with highly obliquely incident waves and alongshore winds. Over 6 h from release, COAWST (coupled ROMS and SWAN, including wave, wind, and tidal forcing) modeled dye compares well with (aerial hyperspectral and in situ) observed dye concentration. Dye first was transported rapidly seaward along the main channel and partially advected across the ebb-tidal shoal until reaching the offshore edge of the shoal. Dye did not eject offshore in an ebb-tidal jet because the obliquely incident breaking waves retarded the inlet-mouth ebb-tidal flow and forced currents along the ebb shoal. The dye plume largely was confined to <4 m depth. Dye was then transported downcoast in the narrow (few 100 m wide) surfzone of the beach bordering the inlet at 0.3 m s^{-1} driven by wave breaking. Over 6 h, the dye plume is not significantly affected by buoyancy. Observed dye mass balances close indicating all released dye is accounted for. Modeled and observed dye behaviors are qualitatively similar. The model simulates well the evolution of the dye center of mass, lateral spreading, surface area, and maximum concentration, as well as regional ("inlet" and "ocean") dye mass balances. This indicates that the model represents well the dynamics of the ebb-tidal dye plume. Details of the dye transport pathways across the ebb shoal are modeled poorly perhaps owing to low-resolution and smoothed model bathymetry. Wave forcing effects have a large impact on the dye transport.

1. Introduction

Tidal inlets are shoreline openings that connect between back-barrier bays, lagoons, marshes, and tidal creeks to the coastal ocean [e.g., *Hayes and FitzGerald*, 2013]. Strong tidal inlet flow (>1 m s^{-1}) can transport sediments, nutrients, larvae, and pollutants. Over a tidal cycle, tidally induced material exchange affects estuary ecosystems, coastal navigation, fishing, and water quality. Morphology, river discharge rate, tidal prism, and wave climate influence the overall inlet hydrodynamics [e.g., *de Swart and Zimmerman*, 2009; *MacCready and Geyer*, 2010; *Geyer and MacCready*, 2014; *Horner-Devine et al*., 2015]. With strong river flow, stratification becomes important and inlets are more appropriately named estuary inlets. Estuary inlet buoyant plumes formed during ebb [e.g., *Garvine*, 1984] can propagate along-coast 10–100 km [*Rennie et al*., 1999; *Lentz et al*., 2003], with plume thickness affected mixing with ocean water underneath [*McCabe et al*., 2009] and by upwelling or downwelling winds [e.g., *Fong and Geyer*, 2001]. Buoyant plumes, from estuaries with significant river flow, have been modeled [e.g., *Garvine*, 1999; *Chen et al*., 2009] without considering wave effects, and typically focus on mid and far-field effects where the effects of earth rotation are important. *Horner-Devine et al*. [2015] provide a comprehensive overview of the mixing and transport processes of coastal river plumes.

Without river flow and stratification, the hydrodynamics of well-mixed shallow inlets depend on tidal phase [*Hench and Luettich*, 2003], with pressure gradients, advection, tendency, and bottom friction important at various tidal phases or locations. Ebb-tidal flows into the coastal ocean, a component of the time-dependent near field [e.g., *Garvine*, 1982; *Horner-Devine et al*., 2015] have been described with steady turbulent plane jet theory [*Tennekes and Lumley*, 1972; *Joshi*, 1982; *Mehta and Joshi*, 1988] with dynamics governed by a balance between nonlinear advection, lateral mixing, and bottom friction [*Ozsoy and Unluata*, 1982]. In realistic inlets with multiple flow channels, ebb-tidal jet dynamics can be complex with

recirculating eddies and buoyancy effects [*Rogowski et al*., 2014; *Chen et al*., 2015]. Coastal along-shelf currents can modify the ebb-jet and increase exchange [e.g., *Wolanski and Imberger*, 1987; *Chadwick and Largier*, 1999].

Surface gravity waves can strongly affect tidal inlet hydrodynamics. Laboratory studies have shown that nonbreaking onshore-propagating waves arrest and widen an ebb-tidal jet [*Ismail and Wiegel*, 1983]. Including wave effects in bottom stress formulations can affect modeled ebb-tidal jets as they propagate on the inner shelf [*Rogowski et al*., 2014]. Ebb-tidal deltas can induce depth-limited wave breaking, limiting wave propagation into the inlet. Divergence in the wave breaking induced momentum flux (e.g., radiation stress [*Longuet-Higgins and Stewart*, 1964]) forces flow at tidal inlets. Modeling studies on realistic inlets suggest that wave breaking during storms can change the ebb-tidal jet magnitude and direction [*Olabarrieta et al*., 2011]. Tidal currents also affect the inlet wavefield [*Dodet et al*., 2013]. Wave-induced circulations can affect the water exchange between a small semienclosed estuary and the inner shelf [*Delpey et al*., 2014]. During hurricanes with large ($>$5 m) significant wave height, radiation stress divergence are large enough to almost completely arrest the ebb-tide outflow [*Orescanin et al*., 2014]. Wave-induced radiation stress divergences also can significantly affect the subtidal inlet flows [*Bertin et al*., 2009; *Wargula et al*., 2014]. Wave breaking (both depth-limited and whitecapping) also increases turbulence and the vertical mixing in ebb-tidal jets [*Thomson et al*., 2014; *Zippel and Thomson*, 2015; *Gerbi et al*., 2015]. Although the effects of wave breaking has been observationally and numerically studies at well-mixed [e.g., *Bertin et al*., 2009; *Olabarrieta et al*., 2011; *Orescanin et al*., 2014; *Wargula et al*., 2014] and stratified [e.g., *Elias et al*., 2012] inlets, a greater understanding of wave forcing effects on inlet flows is needed.

Tracer releases have been reported in many ocean regions from the surfzone [*Clark et al*., 2010; *Hally-Rosendahl et al*., 2015], to within the Hudson Estuary [*Chant et al*., 2007], to the Antarctic Circumpolar Current [*Tulloch et al*., 2014]. Tracer releases in tidal inlets have not been reported. Inlet ebb-tidal Lagrangian drifter experiments also are rare [*McCabe et al*., 2009; *Spydell et al*., 2015]. Using the COAWST modeling system, surface gravity waves had a significant effect on the modeled unstratified river outflow jet and tracer plume [*Olabarrieta et al*., 2014]. Using the model with idealized geometry and constant river volume flux, larger waves resulted in less offshore tracer transport and far more along-coast tracer spreading as ebb-shoal wave breaking slowed the jet and forced along-coast currents [*Olabarrieta et al*., 2014]. Wave obliquity and wind were not considered. The relative importance of different forcing (tidal, wind, wave, and buoyancy) to ebb-tidal inlet plume evolution and transport processes is not understood. Furthermore, how well models can represent these complex processes is not known. Inlet-released tracer plumes have not been observed and models have not been tested.

Here a 2.2 h long dye tracer release within the New River Inlet (NC) during ebb tide with moderate highly obliquely incident waves, strong alongshore winds, and weak buoyancy input is described. Dye observations were made over 5 h and 9 km from inlet mouth and are compared to a simulated dye tracer plume from a model that includes wave, wind, and tidal forcing, but neglects buoyancy effects. For days with much less obliquely incident waves, the ebb-tidal jet can penetrate $\geq$ 1 km into the inner shelf [*Rogowski et al*., 2014]. For this dye release, the observations and model show that the ebb dye plume is trapped to the ebb-tidal shoal due to wave forcing and propagates downcoast in a wave-driven surfzone and wind-driven inner-shelf alongshore current.

This work is part of the May 2012 RIVET-I experiment [e.g., *MacMahan et al*., 2014; *Rogowski et al*., 2014; *Wargula et al*., 2014; *Spydell et al*., 2015; *Zippel and Thomson*, 2015; *Chen et al*., 2015] sponsored by the Office of Naval Research River Mouth Dynamics Departmental Research Initiative. The 7 May 2012 New River Inlet observations collected during the RIVET-I experiment are described in section 2.1. The coupled wave and current (COAWST-ROMS/SWAN) model and the dye release simulations are described in section 2.2. Qualitative and quantitative model data comparisons of the evolving dye plume are presented in section 3. The results are discussed in section 4, particularly in the context of wave forcing and buoyancy, and summarized in section 6.

2. Methods: Observations and Modeling of the New River Inlet

2.1. Observations of the New River Inlet

Observations of waves, currents, and dye tracer in a tidal inlet and the surrounding coastal ocean were collected at the New River Inlet, North Carolina during May 2012 as part of the RIVET-I experiment [*MacMahan*

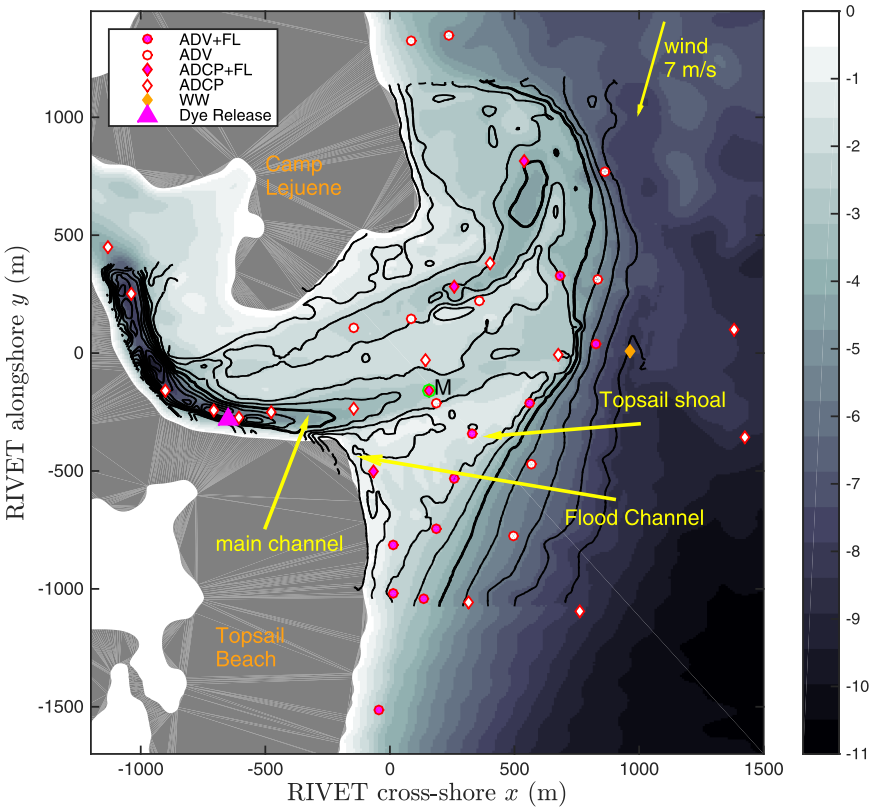

Figure 1. Plan view of the New River Inlet bathymetry as a function of the RIVET cross-shore x and alongshore y coordinates. Land is gray and depth is shaded (in meters) with inlet depth contoured at 1 m intervals with the 4 m depth contour thickened. The Camp Lejuene and Topsail Beach sides of the inlet are noted in orange. The main channel, Topsail shoal, and the flood channel bathymetric features are indicated with yellow arrows. Instrument and dye release locations are indicated by symbols defined in the legend. The colocated ADCP and wirewalker at $(x, y) = (970, 0)$ m is colored orange. The direction and magnitude of the wind on 7 May averaged between $t = 0$ h and $t = 18$ h is indicated in the upper right. The main channel ADCP and fluorometer location at $(x, y) = (157, -158)$ m is marked with an "M."

et al., 2014; *Wargula et al.*, 2014; *Rogowski et al.*, 2014; *Spydell et al.*, 2015; *Zippel and Thomson*, 2015; *Chen et al.*, 2015]. This tidal inlet is on a south-east facing barrier island (Figure 1) with the Marine Corps Base Camp Lejeune on the north-east side and Topsail Beach on the south-west side. A local coordinate system is used with origin in the inlet-mouth center at (latitude, longitude) of $(34.52790^\circ, -77.33823^\circ)$, x increases offshore (at 148° relative to true north), and y increases to the northeast (Figure 1). The inlet is approximately 1000 m wide at the mouth ($x = 0$ m) and narrows to 500 m approximately 500 m upstream of the mouth ($x = -500$ m).

The inlet bathymetry was repeatedly surveyed by the U.S. Army Corp of Engineers from $-1000 < (x, y) < 1000$ m on x parallel lines with 50 m alongshore spacing. Surveyed bathymetry was interpolated to a regular grid (contour lines in Figure 1) and was smoothly embedded into an existing digital elevation model (with 10 m resolution) of the greater New River Inlet region. The inlet bathymetry has an ebb-tidal delta that spans 2000 m alongshore and up to 700 m offshore (Figure 1), and, farther offshore, depth increases rapidly. A "main" navigation channel along the Topsail side (yellow arrow in Figure 1) up to 10 m deep within the inlet shallows to 2 m depth at $x > 100$ m. At $x < -100$ m, the main channel has significant curvature where centrifugal effects may not be negligible. In contrast, at $x > -100$ m, the main channel is nearly straight. The Topsail ebb-tidal shoal is triangular with long straight bathymetry contours (Figure 1). A small flood channel runs between the Topsail shoal and the shoreline (Figure 1).

2.1.1. Fixed Instrumentation

Instruments were deployed within and seaward of the inlet (see legend in Figure 1). Depth-dependent currents were measured with 18 Acoustic Doppler Current Profilers (ADCPs, diamonds in Figure 1) sampling once a minute. Near-bed currents were measured with 22 Acoustic Doppler Velocimeters (ADVs, circles in Figure 1) sampling at 1 or 2 Hz. At all current meter locations, bottom pressure and temperature also were

measured. Fluorometers (WET Labs ECOtripplet) that measure Rhodamine WT dye concentration were deployed at 4 ADCP and 10 ADV locations (filled magenta diamonds and circles, respectively, in Figure 1). A profiling wirewalker mooring (WW) measuring depth and time-dependent temperature, salinity, and Rhodamine WT dye concentration was located offshore of the mouth of the main channel in 8 m water depth (orange diamond in Figure 1). Wave heights and directions were obtained from a Waverider buoy deployed by the US Army Corp of Engineers Field Research Facility in 12 m water depth 6.1 km offshore of the inlet. A meteorological station measured winds on top of a piling at $(x, y) = (-100, -450)$ m. Further details are found elsewhere [*Wargula et al*., 2014; *Spydell et al*., 2015; *Chen et al*., 2015].

2.1.2. 7 May Dye Release and Mobile Dye Measurements

On 7 May 2012, a 21% solution of Rhodamine WT dye was released through a diffuser at $(x, y) = (-652, -281)$ m (magenta x in Figure 1) in 8 m water depth at $z = -5$ m below the surface. A OMEGAFLEX FPU500 Series peristaltic pump pumped a total of 112 L of Rhodamine WT for 139 min from time $t = 12.55$ h to $t = 14.87$ h (12:33–14:52 EDT) at an average flow rate of 13.5 mL s^{-1}.

Surface dye concentration D and temperature T were measured with fluorometers and thermistors mounted on two GPS-tracked jetskis [*Clark et al*., 2009] that sampled the evolving dye field from release ($t = 12.455$ h to $t = 18$ h), spanning the region within the inlet from the dye source downstream, and outside the inlet and up to 6000 m downcoast (–y) in 500 m long cross-shore transects. Offshore of the inlet, temperature, salinity, and dye were measured with small boat CTD+F casts using a Seabird SBE25 CTD and colocated WET Labs fluorometer. Casts spanned from the inlet mouth near $(x, y) = (0, 1000)$ m at $t = 13.5$ h to downcoast near $(x, y) = (-200, -3500)$ m at $t = 17.0$ h. The applied temperature [*Smart and Laidlaw*, 1977] and turbidity [*Clark et al*., 2009] dye corrections are small (<5%).

Hyperspectral and long-wave infrared imagery were recorded on 7 May using the Modular Aerial Sensing System (MASS) developed at Scripps Institution of Oceanography [*Melville et al*., 2016]. Aerial-based near-surface dye was estimated following the instruments and methods described in *Clark et al*. [2014], as summarized below. Dye was imaged using the SIO MASS nadir-looking hyperspectral imager [*Melville et al*., 2016] installed on a Partenavia P68-obs aircraft. The imager is a pushbroom hyperspectral system (SPECIM AisaEagle) in the 400–970 nm range (visible and near infrared), with 5 nm spectral resolution. The FOV is 37.7°, with 944 spatial pixels. Incoming downwelling radiation is measured using a FODIS sensor, synchronized with the hyperspectral camera, allowing hyperspectral measurements to be converted to radiance units. A synchronized, colocated, GPS/INS unit was used to project pixels onto earth coordinates at 1 cm horizontal accuracy. The aircraft flew 47 passes between $t = 12.5$ h and $t = 18.0$ h of 50–250 s duration at altitude between 800 and 1800 m, resulting in hyperspectral pixel resolution of ≤ 1.6 m. Refueling resulted in a data gap between $t = 15.0$ h and $t = 16.3$ h. Aerial-based hyperspectral measurements are converted to dye (in ppb) calibration (of the ratio of radiance at the Rhodamine WT emission and excitation wavelengths) to in situ jetski-based observations for $D < 20$ ppb. Aerial-based dye is accurate to ± 1 ppb for $D = 5$ ppb and ± 4 ppb for $D = 20$ ppb. In addition, surface temperature maps were made by combining long-wave IR camera (FLIR SC6000HS) observations with in situ thermistors.

2.2. Modeling of the Dye Tracer Release

The Coupled Ocean-Atmosphere-Wave-Sediment-Transport modeling system (COAWST) [*Warner et al*., 2010; *Olabarrieta et al*., 2011] was used to simulate the dye tracer release. Here COAWST couples a wave generation and propagation model SWAN (Simulating WAves in the Nearshore) [*Booij et al*., 1999] and an ocean model ROMS (Regional Ocean Modeling System) [*Shchepetkin and McWilliams*, 2005; *Haidvogel et al*., 2000, 2008]. ROMS is a three-dimensional (3D), free-surface, terrain-following numerical model solving the finite difference approximations of the Reynolds-averaged Navier-Stokes (RANS) equations with the hydrostatic and Boussinesq assumptions [*Haidvogel et al*., 2000; *Chassignet et al*., 2000]. Wave forcing and wave-current interaction effects [*McWilliams et al*., 2004; *Uchiyama et al*., 2010] are included. A constant density is used, and thus stratification effects are neglected. A detailed description of the modeling system is found in *Kumar et al*. [2012].

SWAN and ROMS models use the same, nested horizontal curvilinear grids, generated from a high-resolution bathymetric survey near the mouth (from 11 May 2012) and a larger domain digital elevation model (Figure 1). The parent-grid covers the inner estuary and extends offshore about 30 km, to 25 m depth. The mean grid resolution in the inlet area is 60 m, in the offshore region about 300 m, and in the

inner estuary about 15 m. The child-grid, with a factor of 5 higher resolution, spans the inlet and adjacent beaches. The parent and child-gridded bathymetries were smoothed using a second-order Shapiro filter to avoid depth variations large enough to induce pressure gradient errors. This filtering smoothes sharp depth gradients such as the boundary of the main channel and Topsail shoal. Both ROMS grids use five equally spaced sigma vertical layers. SWAN uses a frequency resolution $\Delta f = 0.025$ Hz and 6° directional resolution. The SWAN breaking parameter is set to $\gamma = 0.6$. The ADCIRC database provides the ROMS tidal constituent boundary conditions, which propagate along the open boundaries. ROMS is forced with spatially uniform winds and atmospheric pressure observed at the meteorological station.

ROMS bottom stress is determined by logarithmic layer drag using constant roughness $z_0 = 0.0004$ m, and a k-ϵ turbulence model is used to provide vertical eddy viscosity and tracer diffusivities. For a rough flow regime, the z_0 is equivalent to an effective roughness of 0.012 m associated with bed forms. The associated drag coefficient is within a factor of 2 of a monthlong momentum-balance inferred drag coefficient for the inlet [*Wargula et al.*, 2014]. Lateral eddy viscosity and tracer diffusivity are set to 0.5 $m^2\,s^{-1}$. The ROMS and SWAN parameters and boundary condition application are largely standard [e.g., *Olabarrieta et al.*, 2011; *Kumar et al.*, 2015]. The coupled ROMS-SWAN simulations were performed from 1–21 May 2012 (denoted full-run), with a spin-up period prior to 1 May. The full-run SWAN offshore boundary conditions were derived from the NOAA database of operational output (WAVEWATCH III version 2.22 hindcast). Observed winds were used to generate waves within the parent and child SWAN grids. The COAWST full-run will be compared to wave and current observations elsewhere.

To simulate the 7 May dye release, the child-grid was rerun for 7 May from midnight to 2000 EDT hours (denoted dye-run). The dye-run used the full-run child-grid for initial conditions, and the full-run parent-grid for boundary conditions. This run also used the observed waves at the FRF Waverider buoy 6 km offshore as child-grid SWAN boundary condition. The measured significant wave height, peak period, and peak direction were used to define JONSWAP wave spectra applied as the dye-run boundary conditions on all open boundaries, updated every half an hour. Results did not change significantly if parent-run wave boundary conditions were used. All other dye-run model parameters were identical to those for the full-run. Model dye was released continuously as a bottom source at a grid location closest to the actual dye release. The observed and model dye release timing, dye flow rate, and total dye mass are identical. Model tracer boundary conditions were set to radiating, allowing dye to leave the model domain.

3. Results: Model Data Comparison

On 7 May, from $t = 0$ h to $t = 20$ h, the wind speed varied between 6 and 10 $m\,s^{-1}$ with direction veering from alongshore (from $+y$, 90°) to side-onshore (from 45°). The 7 $m\,s^{-1}$ average wind was side-onshore (yellow arrow in Figure 1). During the daytime, the significant wave height H_s in 13 m water depth (6 km offshore) varied from 0.9 m to 1.3 m with peak periods of approximately 6 s, and mean wave angles varying from 25° to 40° (positive implies waves coming from $+y$). Thus, the wind and the wavefield were coincident.

3.1. Main Channel: Tidal Elevation, Currents, and Dye

Within the main channel at location M [$(x, y) = (157, -158)$ m with $h = 2.6$ m water depth relative to mean sea level (Figure 1)], the observed tides are largely semidiurnal, with a high ($\eta = 0.84$ m) at $t = 8.8$ h and a low ($\eta = -0.6$ m) at $t = 15.0$ h (Figure 2a, blue curve), where η is the sea surface elevation relative to mean sea level. The modeled sea surface generally simulates well the timing and amplitude of the observed tide, although with 0.15 m low bias throughout (Figure 2a, red curve). The observed and modeled depth-averaged along-channel velocities U_c are largely in phase with the tide (Figure 2b, blue curve), indicative of the progressive character of the tide at New River Inlet [*MacMahan et al.*, 2014]. The observed peak flood $U_c = -0.41$ $m\,s^{-1}$ at $t = 8.2$ h and peak ebb $U_c = 1.25$ $m\,s^{-1}$ at $t = 14.5$ h are modeled well, to within 0.01 $m\,s^{-1}$ and 0.15 h of the observed (red curve in Figure 2b). During the flood-to-ebb transition ($t = 10$–12 h), observed and modeled channel velocity have the largest difference (about 0.28 $m\,s^{-1}$). However, during the observational period ($t = 12.5$ h to $t = 20$ h), the observed and modeled U_c closely agree (errors 0.08 $m\,s^{-1}$), and the ebb-to-flood transition at $t = 18.08$ h is simulated accurately (compare red and blue in Figure 2b). At $t = 12.83$ h, shortly after the $t = 12.55$ h dye release start, dye is observed at station M (Figure 2c, blue curve), 819 m downstream of the dye release. With some variability, the observed dye increases to a 4 ppb maximum at $t = 14.5$ h, shortly

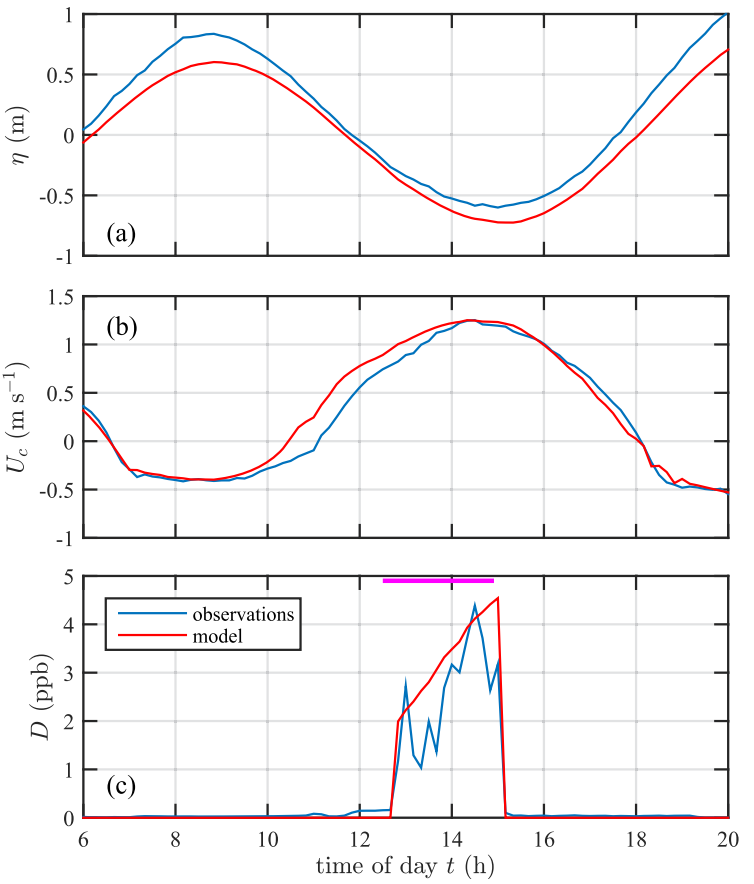

Figure 2. (a) Sea surface elevation η (relative to mean sea level), (b) along-channel velocity U_c, and (c) dye D versus time of day (hours) on 7 May 2012 at instrument M [$(x, y) = (157, -158)$ m in Figure 1] in $h = 2.6$ m depth (relative to mean sea level) for the observations (blue) and model (red). In Figure 2c, the magenta bar indicates the duration of the dye release.

before the dye release ends, and then decays rapidly to zero by $t = 15.17$ h, 20 min after the dye release ends. The observed and modeled dye are similar (errors of 0.8 ppb), although the model dye has less variability (Figure 2c, red curve).

3.2. Surface Dye Model Data Comparison

Qualitatively, the observed and modeled 7 May surface dye field agree well (Figures 3–7). The evolution of the dye field is broken down into the near, mid, and far field. In the near field, within 0.8 h ($t \leq 13.33$ h) of the dye release start ($t = 12.55$ h), dye is largely contained near the inlet ($y > -1200$ m, Figure 3). Initially, observed dye at 10–15 ppb is transported offshore along the main channel, although some dye at 5 ppb is transported over the southern shoal (Figures 3a and 3c). The model dye is similar, although too strong over Topsail shoal and in the near-shoreline flood channel (Figures 3b and 3d). Observed dye exits the main channel and mostly turns right and advects downcoast ($-y$) along the offshore part of Topsail shoal (Figures 3e, 3g, and 3i). Dye is not ejected in a jet offshore of the main channel. The model dye is qualitatively similar to observed (Figures 3f, 3h, and 3j), particularly the downstream dye leading edge and dye plume cross-shoal extent. However, the model dye is spatially smoother than observed.

The midfield (Figures 4 and 5) is defined as times when significant dye is present both within and outside the inlet during the dye release or shortly after it ends. Early in the midfield as the dye release continues ($13.48 \leq t \leq 13.97$ h), observed dye is advected out the main channel and over Topsail shoal, and is transported downcoast ($-y$) at about 5 ppb up to 2 km from the inlet center (Figures 4a, 4c, and 4e). Observed dye is not ejected offshore in an ebb-tidal jet, but is mostly contained within the 4 m depth contour with some dye out to 6 m depth. The model dye field during this time is similar to the observed (Figure 4, right), particularly the cross-shore extent and the downstream leading edge. However, the modeled dye is at higher concentrations and less patchy than observed.

Later in the midfield, the qualitative model data comparison continues to be quite good (Figure 5). At 2 h after the dye release started ($t = 14.53$ h), observed and modeled dye continues to advect along the main channel, spread across Topsail shoal, and transport downcoast (Figures 5a and 5b). Significant observed dye is not ejected offshore of the main channel. The downcoast leading dye edge is near $y = -3000$ m in a 200 m wide plume at 3 ppb that widens to 500 m toward Topsail shoal at 5–10 ppb. Between $-2000 < y < -500$ m, the observed dye has eddy-like alongshore variability with scales of about 300 m, and most observed dye is contained within the 6 m depth contour (Figure 5a). The model dye is similar (Figure 5b); however, model nearshore (≤ 2 m depth) dye concentration is too elevated

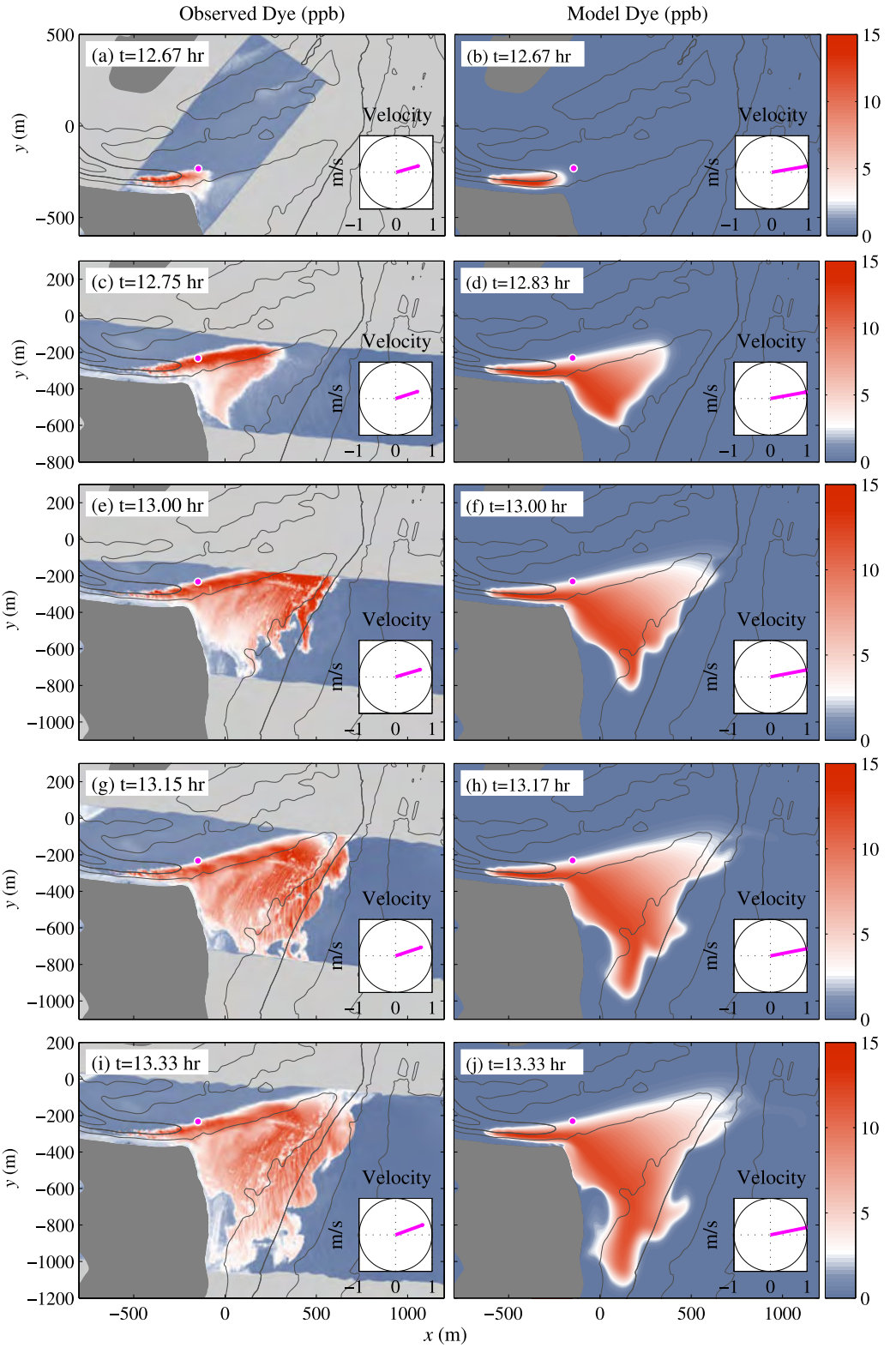

Figure 3. Near-field (left) observed and (right) modeled surface dye (ppb) with bathymetry (2, 4, 6, and 8 m) contours as a function of cross-shore x and alongshore y coordinate for times $t \leq 13.33$ h (within 0.8 h of the dye release start). Each row represents a specific observation time with closest model time given in the upper left inset. Velocity magnitude and direction (magenta line, inset, bottom right corner) is from inlet location $(x, y) = (-148, -233)$ m (magenta dot). Land is indicated with dark gray, and in the observed panels (left) regions outside aerial observations are indicated in light gray. The 4 m contour is slightly thickened.

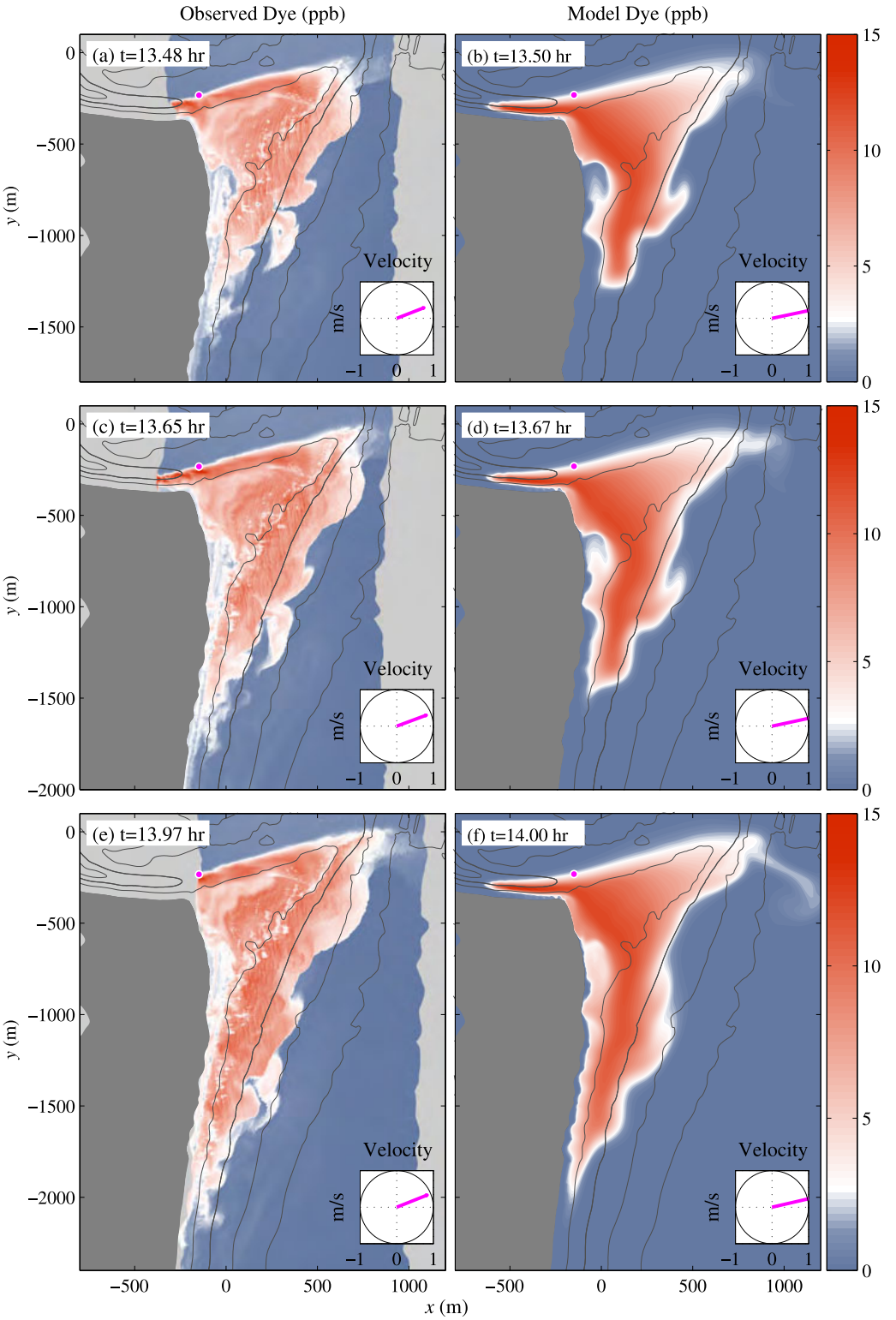

Figure 4. Early midfield (left) observed and (right) modeled surface dye from (top, a, b) $t = 13.48$ h to (e, f, bottom) 14.0 h. Figure details are as described in Figure 3.

without the observed eddy-like variability. At 0.5 h later ($t = 15.0$ h), the dye release has ended and the observed dye field continues to advect downcoast now beyond $y = -4000$ m with a distinct trailing edge (Figure 5c). The model dye plume is similar to the observed (Figure 5d), although the downcoast

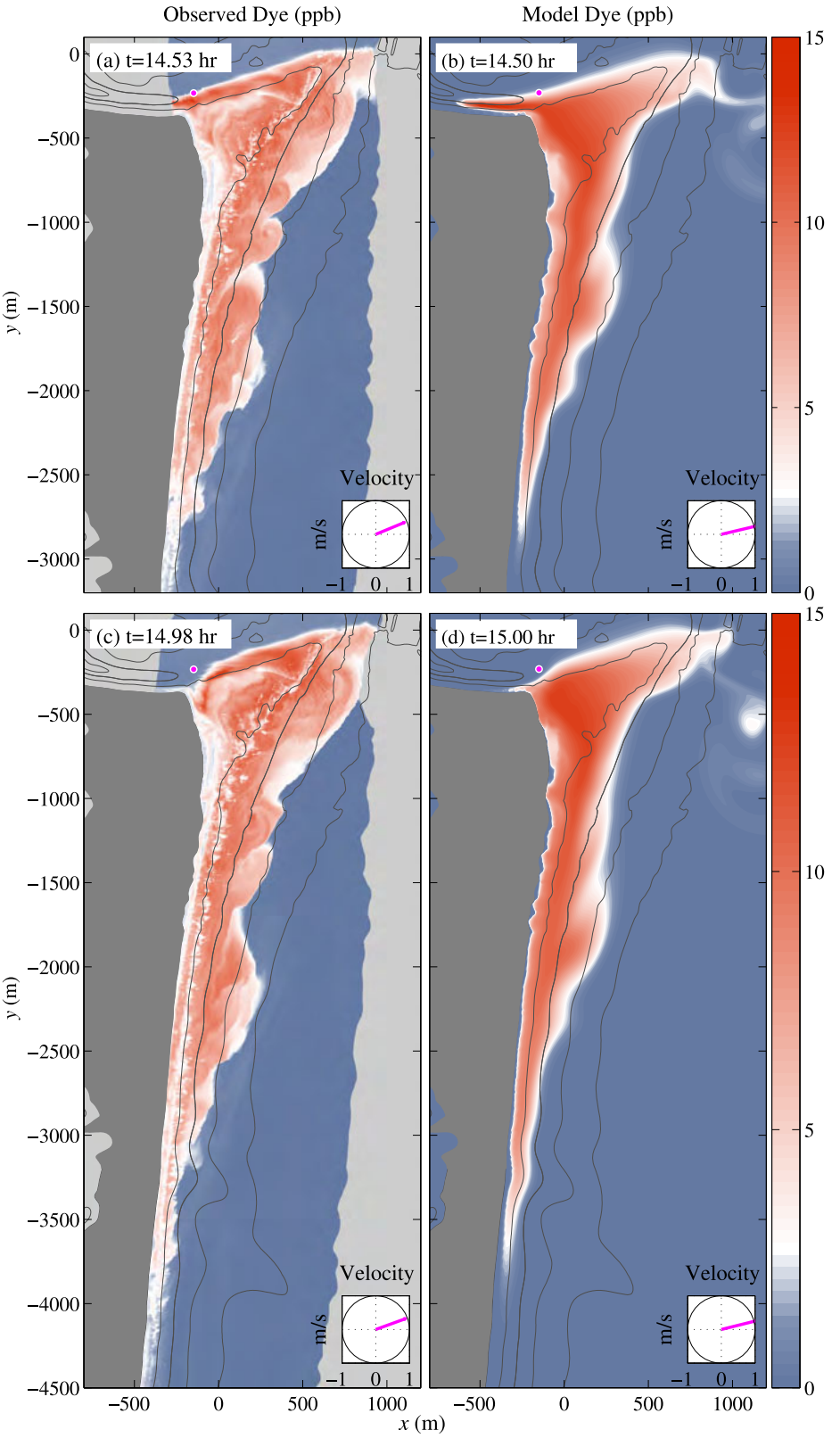

Figure 5. Later midfield (left) observed and (right) modeled surface dye from (a, b) t = 14.5 h to (b, c) t = 15.0 h. Figure details are as described in Figure 3.

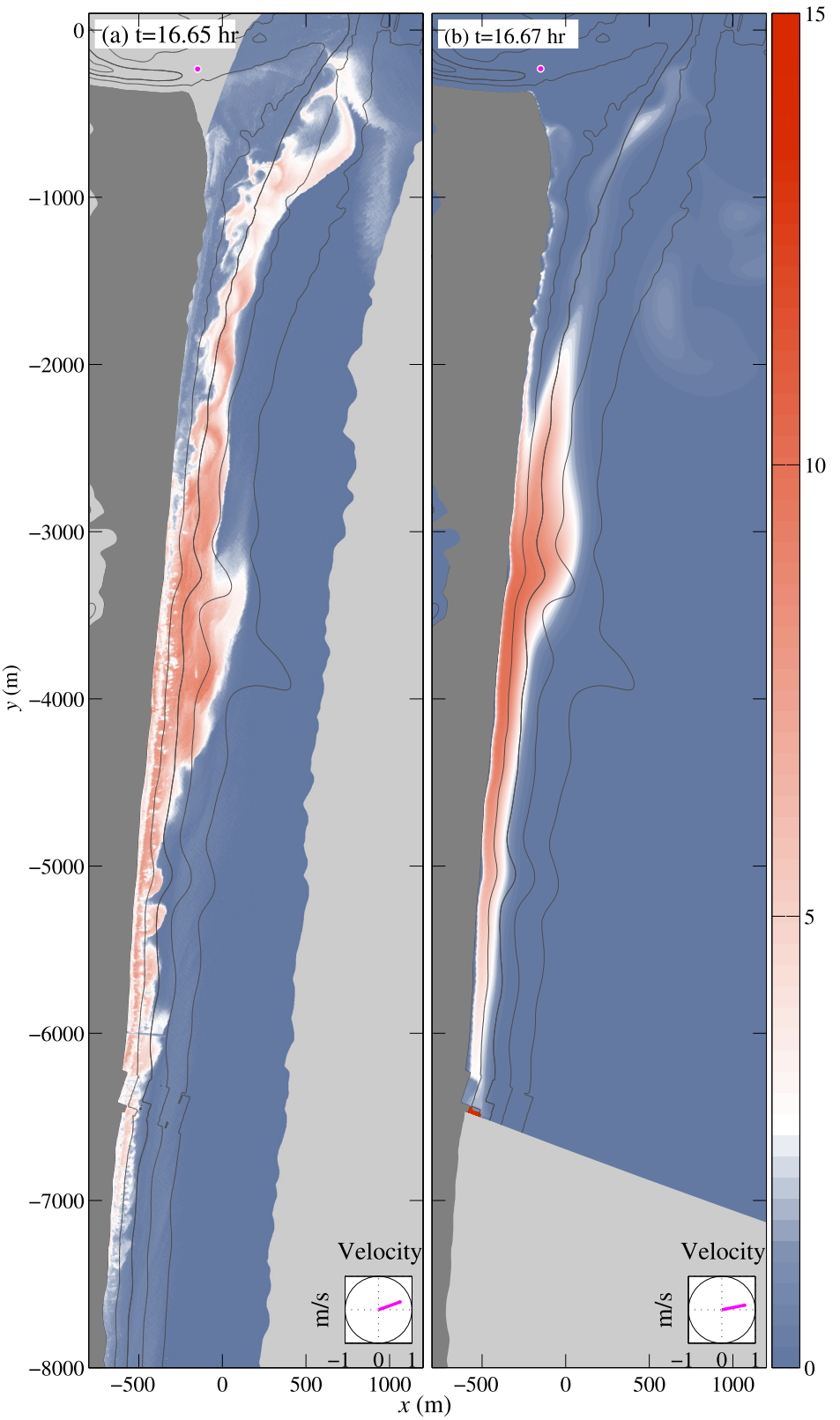

Figure 6. Far-field (left) observed and (right) modeled surface dye at time t = 16.67 h. Figure details are as described in Figure 3.

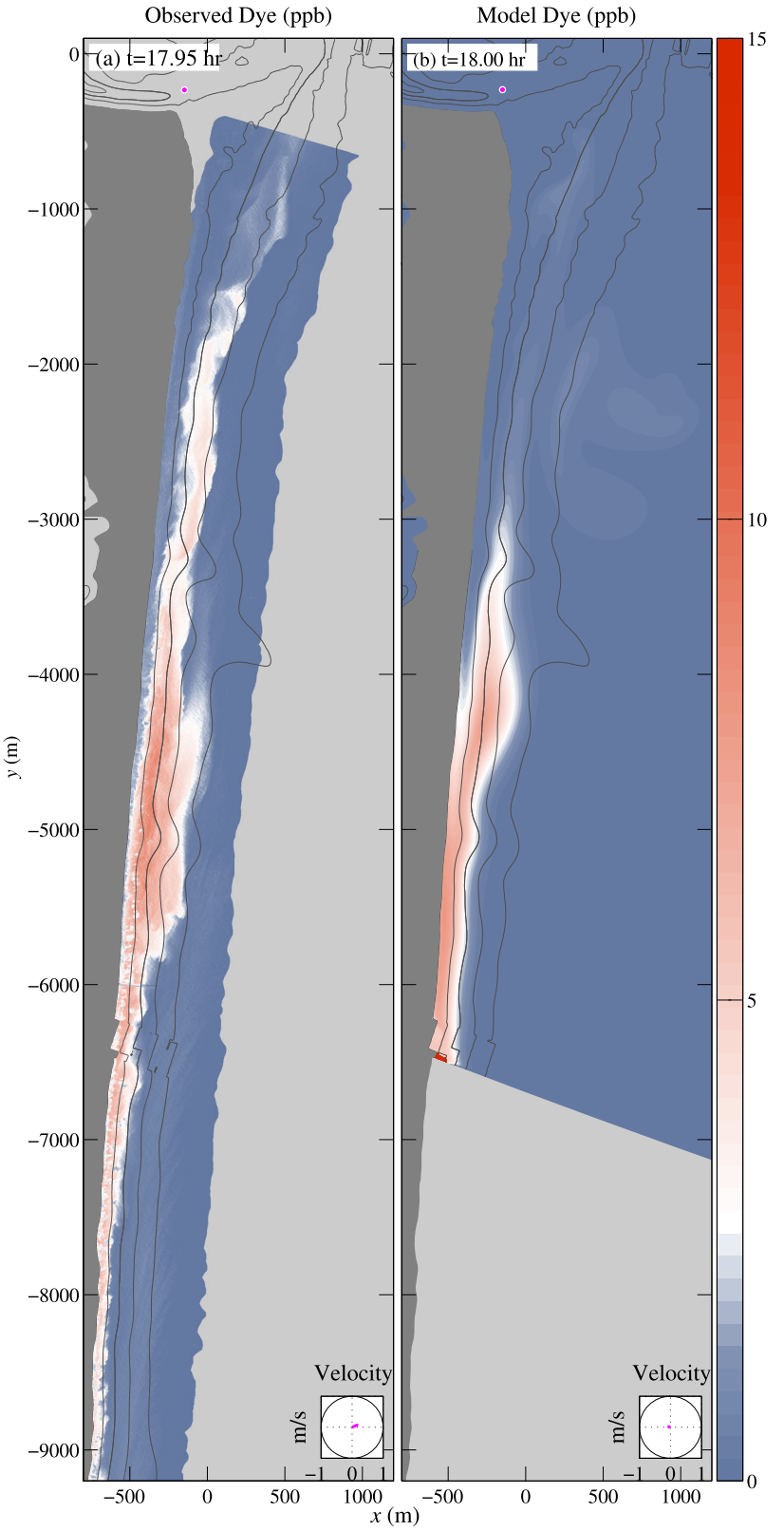

Figure 7. Far-field (left) observed and (right) modeled surface dye at time t = 18 h. Figure details are as described in Figure 3.

advection rate is slower than observed, the nearshore concentrations is elevated, and the plume width is narrower.

The aerial observations have a gap from $t = 15.0$ h to $t = 16.35$ h, during which dye was fully transported out of the inlet and continued downcoast. The time period ($t \geq 16.35$ h) where dye has left the inlet is denoted the far field (Figures 6 and 7) and includes the transition from ebb to slack flow within the inlet. Early in the far field at $t = 16.65$ h (4 and 1.8 h from the dye release start and end, respectively), observed dye has spread out about 7 km alongshore to $y = -7300$ m (Figure 6a), with dye concentrations from 2 to 10 ppb. The leading 2500 m of the dye patch is shoreline-attached, narrow (100–200 m wide) at <5 ppb, with some alongshore structure at 200 m scales. Toward the inlet, the dye patch has a 500 m wide bulge between $-4500 < y < -3300$ with 5–10 ppb dye concentrations. The dye patch trailing edge at $y > -1800$ m is detached from the shoreline, but mostly is contained between the 4 and 6 m isobaths with weaker dye concentrations (<5 ppb) and eddy-like spatial variability.

The child model grid extends to only $y = -6300$ m (light gray shading in Figures 6b and 7b), limiting detailed model data comparison. Nevertheless, the model dye patch is qualitatively similar to the observed. At $t = 16.67$ h, the model dye leading edge at $y < -5000$ m (Figure 6b) has width and concentration similar to observed, although with less structure. The model dye also has a 500 m wide dye patch bulge between $-3600 < t < -2600$ m at 5–10 ppb, similar to the observed, although displaced +500 m alongshore. The model dye trailing edge also disconnects from the shoreline, but is more diluted (mostly <2 ppb) than observed, with less spatial variability.

Later in the far field at $t = 18.0$ h, the observed and modeled inlet mouth is at slack tide, and dye has been transported farther downcoast with similar observed and modeled spatial structure (Figure 7). The observed dye has now spread over 8 km alongshore beyond $y = -9000$ m in an elongated, narrow (mostly 200 m wide), largely shoreline-attached, coherent patch (Figure 7a). The 500 m wide bulge has advected downcoast to $-5800 < y < 4200$ and widened alongshore, indicating shear dispersion. The 2400 m long dye patch trailing edge also is shoreline detached and remains contained mostly between the 4 and 6 m depth contour. Although the model grid does not extend that far downstream, at $t = 18.0$ h, the model and observed dye features are similar where there is overlap (Figure 7b).

3.3. Surface Dye Moments Model Data Comparison

The qualitative model data surface dye D_s agreement (Figures 3–7) now is quantified using observed and modeled surface dye D_s moments. Surface dye center of mass (first moments) $(\bar{X}, \bar{Y})$ are calculated via,

$$\bar{X}(t) = D_0^{-1} \int\int x D_s(x, y, t)\, dx\, dy, \tag{1}$$

$$\bar{Y}(t) = D_0^{-1} \int\int y D_s(x, y, t)\, dx\, dy, \tag{2}$$

where D_0 is the zeroth surface dye moment,

$$D_0(t) = \int\int D_s(x, y, t)\, dx\, dy. \tag{3}$$

Surface dye lateral spreading is quantified with the second moment tensor C with components

$$C_{xx}(t) = D_0^{-1} \int\int (x - \bar{X})^2 D_s(x, y, t)\, dx\, dy, \tag{4}$$

$$C_{yy}(t) = D_0^{-1} \int\int (y - \bar{Y})^2 D_s(x, y, t)\, dx\, dy, \tag{5}$$

$$C_{xy}(t) = D_0^{-1} \int\int (x - \bar{X})(y - \bar{Y}) D_s(x, y, t)\, dx\, dy. \tag{6}$$

A surface dye second-moment area σ^2 is

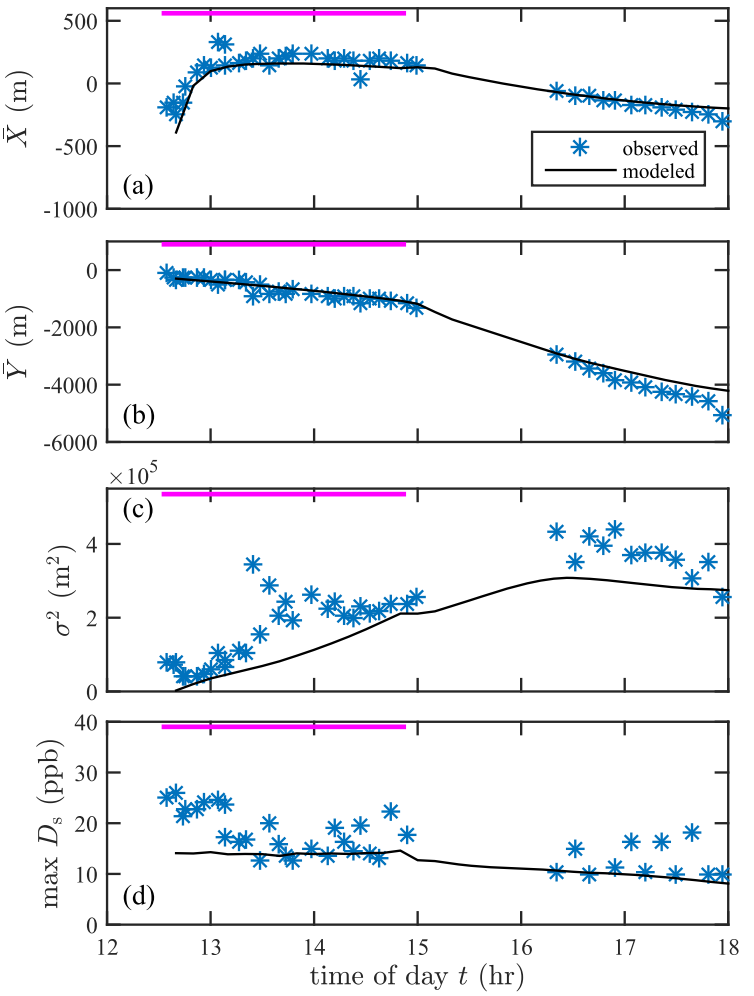

Figure 8. Observed (asterisks) and modeled (black curves) surface dye moments versus time of day: dye center of mass (a) $\bar{X}$ (1) and (b) $\bar{Y}$ (2), (c) second-moment area σ^2 (7), and (d) maximum D_s. In all figures, the magenta bar indicates the duration of the dye release.

$$\sigma^2 = \lambda_1 \lambda_2, \tag{7}$$

where $\lambda_{1,2}$ are eigenvalues of C. The maximum dye D_{max} (i.e., infinity norm) is used to quantify dye dilution. The observed moment integrals (1–4) are calculated over the imaged region in each aerial pass (Figures 3–7). To reduce bias, moments are calculated only for aerial passes that imaged most of the surface dye field, potentially introducing some noise or bias. The modeled moments are integrated over the entire modeled domain and have bias for $t > 16.0$ h because the model domain ends at $y \approx -6300$ m.

Overall, the model accurately simulates the ($\bar{X}$, $\bar{Y}$) surface dye center of mass (Figures 8a and 8b). For 0.5 h from release start, the observed and modeled $\bar{X}$ move offshore about 500 m as dye is transported out of the inlet (Figure 3). As dye turns downcoast, observed and modeled $\bar{X}$ decreases slowly to ≈ -300 m at $t = 18.0$ h and $\bar{Y}$ decreases from ≈ 0 m at $t = 13.0$ h to $\bar{Y} \approx -5000$ m at $t = 18.0$ h. In the far field with no dye in the inlet ($t > 16.35$ h), $d\bar{Y}/dt$ implies a downcoast advection rate of 0.3 m s^{-1} (Figure 8b). The $\bar{X}$ and $\bar{Y}$ model data rms errors are relatively small (87 and 158 m, respectively). Modeled $\bar{Y}$ bias is evident for $t > 17.0$ h as model dye leaves the domain. The model simulates reasonably well the overall observed second-moment area σ^2 (Figure 8c), although the model is biased low with too little variability. For $t \leq 15.0$ h, both observed and modeled dye area grow roughly linearly, consistent with asymptotic shear dispersion [*Taylor*, 1953]. In the far field ($t > 16$ h), both observed and model σ^2 are roughly constant, indicating weak diffusion. During the dye release ($12.55 < t < 14.87$ h), the observed maximum D_s is noisy (as expected) between 15 and 25 ppb and occurs close to the dye release (Figure 8d). The modeled maximum D_s is essentially constant, as expected. After the dye release ends, observed and modeled dye dilutes slowly with maximum D_s of 10 ppb at $t = 18.0$ h, with the model biased low (Figure 8d). This slow far-field dye dilution is consistent with slow σ^2 spreading (Figure 8c).

3.4. Inlet and Ocean Dye Mass and Transport: Model Data Comparison

Next the evolution of observed and modeled dye mass (in ppb m^3) from the "inlet" to the "ocean" regions are presented. The "inlet" and "ocean" regions are separated (yellow dashed curve in Figure 9) by the 4 m depth contour (relative to mean sea level), cutoff at $y = -1500$ m where a current meter and fluorometer (magenta circle at $y = -1500$ m) were colocated. Thus, the "inlet" region contains Topsail shoal. The dye mass (M) for the "inlet" (M_{in}) and "ocean" (M_{oc}) regions are

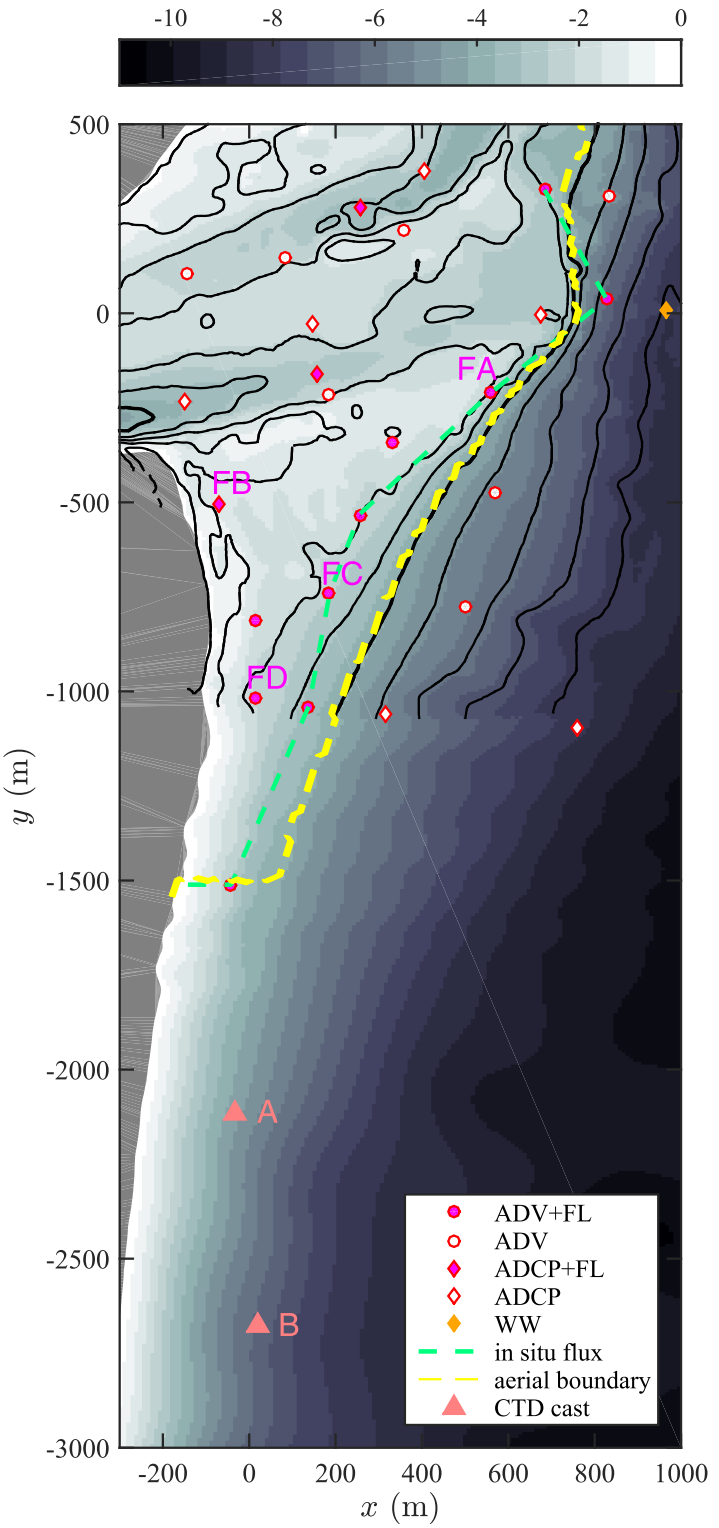

Figure 9. Plan view of the New River Inlet bathymetry as a function of the RIVET cross-shore x and alongshore y coordinates as in Figure 1. Land is gray and depth is shaded (in meters) with inlet depth contoured at 1 m intervals. Instrument locations are indicated by symbols with instrument types in the legend. The yellow dashed curve represents the border between the "inlet" and "ocean" regions, primarily on the $h = 4$ m contour. The green dashed curve represents the in situ flux integration path (14). The two triangles (A and B) mark CTD cast locations (Figure 10). Specific in situ fluorometer locations are marked FA-FD.

$$M_{\mathrm{in,oc}}(t) = \int\int_{\mathrm{in,oc}} \int_{-h}^{\eta} D(x,y,z,t)\,\mathrm{d}z\,\mathrm{d}x\,\mathrm{d}y, \quad (8)$$

where the horizontal integral is over the inlet (in) or ocean (oc) region (Figure 9). The total (inlet + ocean) dye mass is $M_{\mathrm{tot}} = M_{\mathrm{in}} + M_{\mathrm{oc}}$. The model inlet and ocean dye mass is calculated from the 3-D model dye field.

Although the aerial observations provide good spatial coverage (Figures 3–7), detailed vertical dye structure observations to directly calculate the vertical integral in (8) are lacking. Instead, a vertical dye scale [i.e., *Hally-Rosendahl et al.*, 2015] is estimated from 30 CTD + Dye casts collected between 13.2 and 17.5 h outside the inlet in 4–7 m water depth, typically along the offshore dye field edge as it advected downcoast. Two example CTD + Dye casts are shown in Figure 10. At location A $[(x,y) = (-32, -2115)$ m] in $h = 4$ m at $t = 16.6$ h, the observed dye has weak vertical variation (from 5 ppb at $z = -1$ m to 3.5 ppb at $z \approx -3.5$ m), coincident with the weak temperature and salinity vertical variations (blue curves in Figures 10b and 10c). Slightly (0.2 h) later, at the deeper ($h = 5.5$ m) downstream location B $((x,y) = (17, -2679)$ m), the observed dye varies 1–2 ppb above $z = -3.5$ m, and is zero below $z = -3.5$ m, coincident with a temperature and salinity-induced pycnocline (red curves in Figure 10). At locations A and B (and throughout the domain), model dye is largely vertically uniform (dashed curves in Figure 10), as the model has no temperature or salinity structure.

Following *Hally-Rosendahl et al.* [2015], the vertical dye integral is related to the observed surface dye via

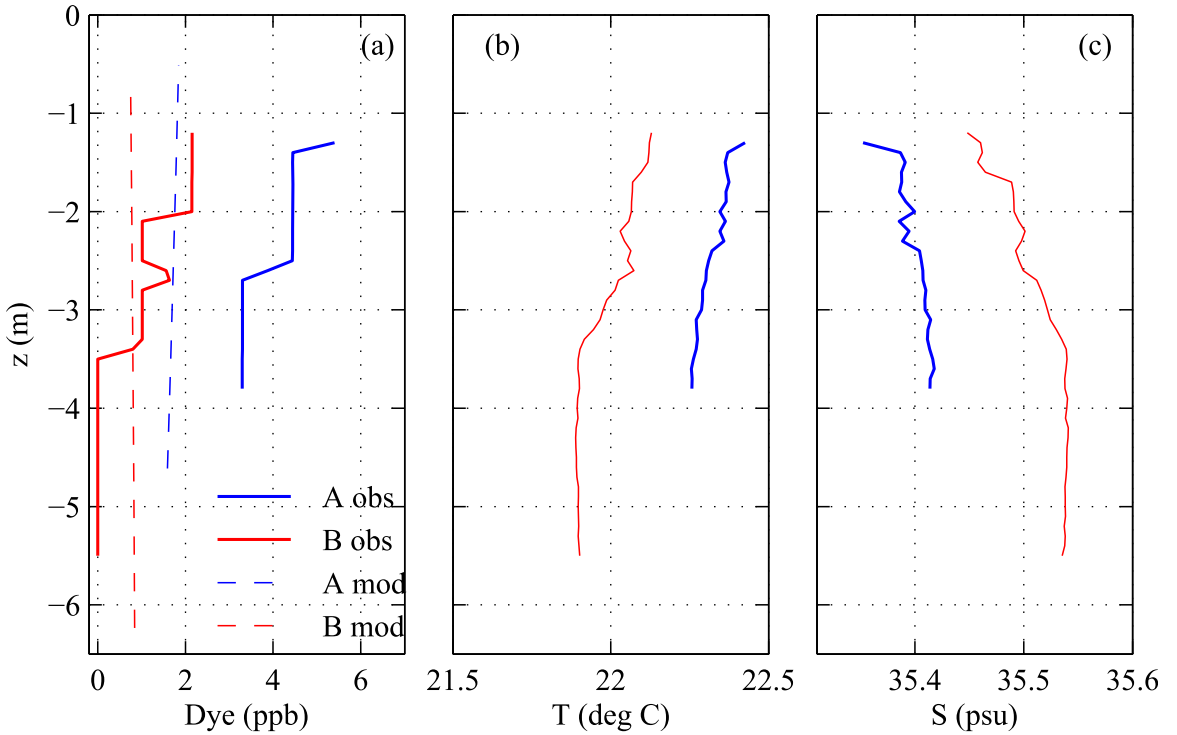

Figure 10. (a) Dye, (b) temperature T, and (c) salinity S versus depth z for two CTD casts (red and blue) marked A and B in Figure 9. In Figure 10a, the dashed lines show the model dye at each cast.

$$\int_{-h}^{\eta} D(z)\,\mathrm{d}z = h_{\mathrm{dye}} D_s, \tag{9}$$

where h_{dye} is a vertical dye scale and D_s is the surface dye concentration. The average (over all casts) results in $h_{\mathrm{dye}}=3.5$ m. The vertical dye integral (9) is used to calculate $M_{\mathrm{in,oc}}^{(\mathrm{obs})}$, with h_{dye},

$$h_{\mathrm{dye}} = \begin{cases} h, & \text{for } h < 3.5\,\mathrm{m} \\ 3.5\ \mathrm{m}, & \text{for } h \geq 3.5\,\mathrm{m}. \end{cases} \tag{10}$$

For the observed dye mass, the horizontal integral in (8) is over the region imaged by each aerial pass.

The aerial-observed total dye mass $M_{\mathrm{tot}}^{(\mathrm{obs})}$ balances the total released dye,

$$M_{\mathrm{tot}}(t) = \int_{t_0}^{t} Q_{\mathrm{rel}}\,\mathrm{d}\tau, \tag{11}$$

where the dye release rate Q_{rel} is constant during release and zero thereafter (Figure 11a). During the dye release (early and midfield), $M_{\mathrm{tot}}^{(\mathrm{obs})}$ increases linearly, slightly (13%) faster than the dye pump rate. In the far field ($t > 16.35$ h, Figure 7), $M_{\mathrm{tot}}^{(\mathrm{obs})}$ is roughly constant with average within 10% of the total released dye $M_{\mathrm{rel}} = 2.33\times10^7$ ppb m^3 (Figure 11a). The total mass budget (11) closure shows that the dye mass estimation method is accurate over 5 h from release start and with dye transported 9 km downcoast.

Similar to the surface dye center of mass, area, and maxima (Figure 8), the time evolution of the inlet and ocean dye mass is modeled well (Figure 11b). The observed and modeled inlet dye mass ($M_{\mathrm{in}}^{(\mathrm{obs})}$ and $M_{\mathrm{in}}^{(\mathrm{m})}$) increase linearly from the dye release start at $t = 12.5$ h until $t \approx 14.0$ h, equilibrating at $M_{\mathrm{in}}^{(\mathrm{obs})} \approx 10^7$ ppb m^3 until the dye release ends at $t = 14.8$ h (Figure 11b, compare black asterisks and curve). By $t = 13.0$ h, the observed ocean dye mass $M_{\mathrm{oc}}^{(\mathrm{obs})}$ begins to increase in an accelerating manner, with strongest increase as $M_{\mathrm{in}}^{(\mathrm{obs})}$ equilibrates (Figure 11b, red diamonds). The model ocean dye mass $M_{\mathrm{oc}}^{(\mathrm{m})}$ is similar to, but lags $M_{\mathrm{oc}}^{(\mathrm{obs})}$ by about 0.3 h (Figure 11b, red curve).

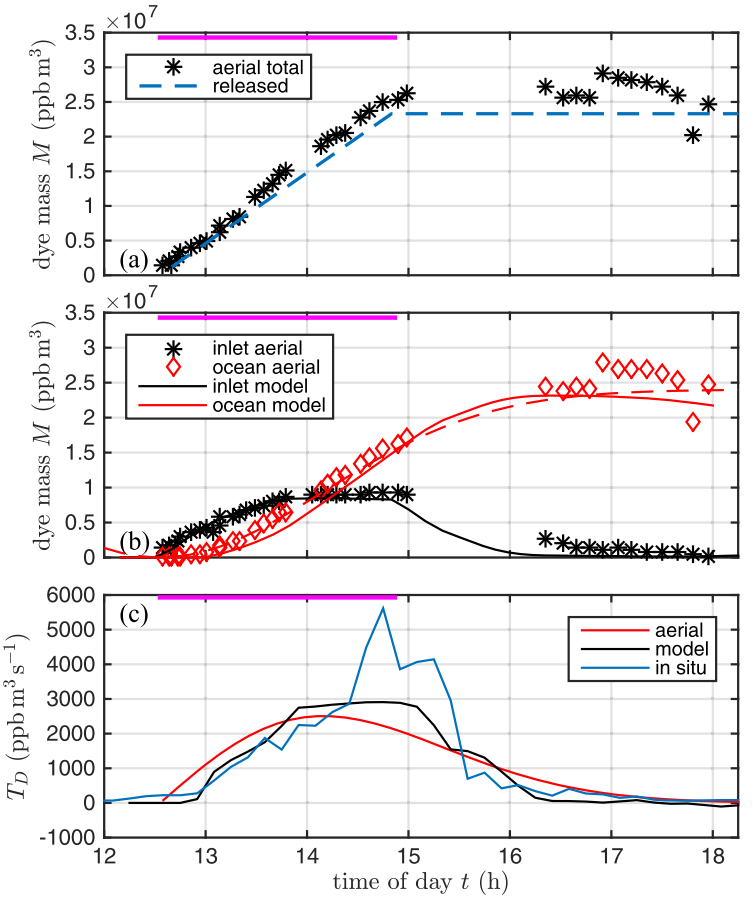

Figure 11. (a) Total (inlet + ocean) aerial-observed dye mass M_{tot} (black asterisk) and total released dye (blue dashed) versus time. The total dye released $M_{rel}=2.33\times10^7$ ppb m^3. (b) Ocean M_{oc} (red) and inlet M_{in} (black) dye mass versus time for aerial-observed (symbols) and modeled (curves). The best fit functional form (13) aerial-observed ocean $M_{oc}^{(obs)}$ is given by the red dashed curve. (c) Dye transport T_D from inlet to ocean versus time for the in situ (blue), aerial observed (red), and model (black). In all figures, the magenta bar indicates the duration of the dye release.

After the dye release ends and once the aerial observations restart ($t=16.35$ h), observed $M_{in}^{(obs)}$ is reduced 80% and continues to decay linearly to zero at $t=18.0$ h. The far-field model $M_{in}^{(m)}$ is similar to, but decays more rapidly than observed ($M_{in}^{(m)}=0$ by $t=16.5$ h) due to the long observed dye tail at $y>-2000$ m (e.g., Figures 6a and 6b). At $t\geq16.0$ h, the observed ocean dye mass $M_{oc}^{(obs)}$ is scattered near the total dye mass released $M_{rel}=2.4$ ppb m^3 (compare red diamonds and blue dashed curve in Figure 11b). The model ocean dye mass $M_{oc}^{(m)}$ is similar to observed, equilibrating to M_{rel} by $t=16.0$ h, and decaying slowly thereafter as dye mass leaves the child model grid near $y=-6300$ m (see Figures 6b and 7b).

The tracer transport $T_D(t)$ from the "inlet" to the "ocean," delineated by the yellow dashed boundary in Figure 9, is estimated in three ways. As the dye source is within the inlet, $T_D(t)$ is

$$T_D(t)=\frac{dM_{oc}}{dt}. \tag{12}$$

Model $T_D^{(m)}$ and aerial-observed $T_D^{(obs)}$ are directly estimated with (12). However, $M_{oc}^{(obs)}$ are noisy and are fit to a smooth empirical functional form

$$\hat{M}_{oc}^{(obs)}=M_{rel}\left[1-\exp\left(-\frac{(t-t_0)^2}{\tau^2}\right)\right], \tag{13}$$

where $M_{rel}=2.33$ ppb m^3 is the total released dye, with best fit parameters $t_0=12.552$ h and $\tau=2.28$ h. The fit $\hat{M}_{oc}^{(obs)}$ and observed $M_{oc}^{(obs)}$ agree well (compare red dashed and red diamonds in Figure 11b), and $\hat{M}_{oc}^{(obs)}$ is used to calculate transport $T_D^{(obs)}$ from (12). The in situ dye transport from inlet to ocean is estimated on a nearby contour connecting the in situ instruments (green dashed line in Figure 9). Assuming vertically well-mixed D and mean velocity $\mathbf{U}$ at these relatively shallow locations, the in situ dye transport $T_D^{(is)}(t)$ is

$$T_D^{(is)}(t)=\int_C hD\mathbf{U}\cdot\mathbf{n}\,dl, \tag{14}$$

where the line integral is over the in situ transport contour (green dashed in Figure 9) and $\mathbf{n}$ is the unit outward normal. The in situ $T_D^{(is)}$ is estimated with 1 min averaged h, D, and $\mathbf{U}$, and is subsequently averaged over 20 min.

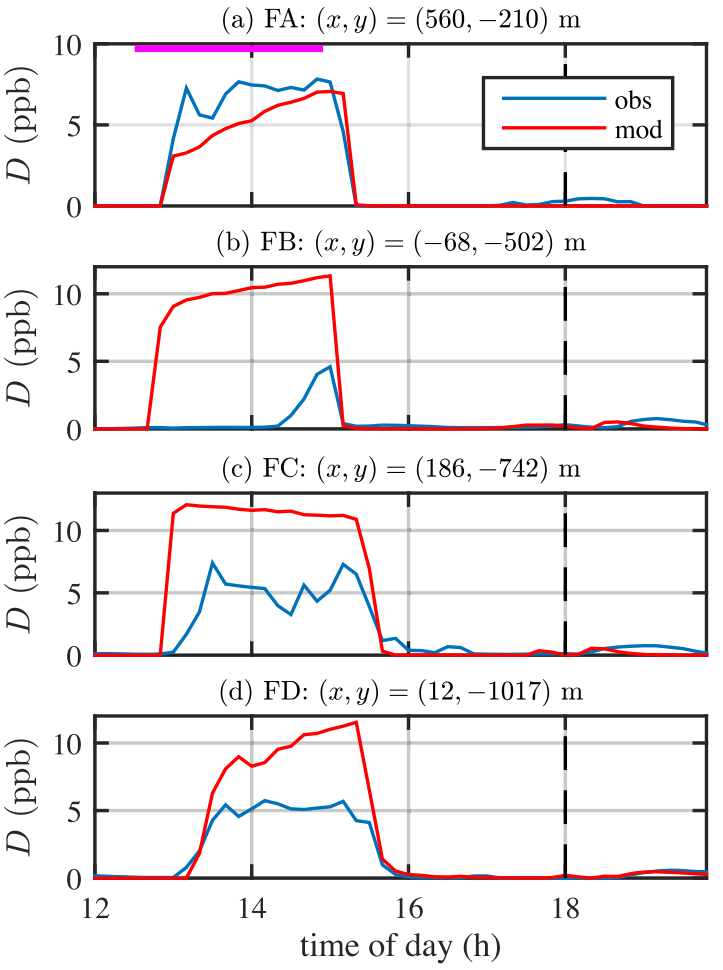

Figure 12. Observed (blue) and modeled (red) dye D versus time of day in hours for Topsail shoal fluorometer locations (a) FA to (d) FD indicated in Figure 9 and with (x, y) locations given in each figure. The vertical dashed line indicates the time of inlet slack tide in the ebb to flood transition. In Figure 12a, the magenta bar indicates the dye release duration.

The in situ, aerial observed, and modeled T_D agree qualitatively, ramping up to a maximum and decreasing after the dye release ends (Figure 11c). Aerial observed and modeled T_D have similar maximum near $T_D =$ 2500 ppb m^{3}s^{-1}. The in situ $T_D^{(is)}$ is similar to the observed and modeled early in the release, but between 14.5 and 15.5 h, at the lowest tide and maximum ebb (Figure 2), the $T_D^{(is)}$ is elevated and noisy relative to the aerial-observed and modeled T_D. This likely results from the instrument spacing (250–500 m) not sufficiently resolving the dye field. Overall, the net in situ transport is accurate. The ratio of net transport to released dye,

$$\frac{\int T_D^{(is)}\, dt}{M_{rel}} = 1.18,$$

is near-one indicating that the in situ current meter and fluorometer array adequately sampled the overall dye field.

3.5. Fixed Location Model Comparison

Given the good qualitative (Figures 3–7) and quantitative (Figures 8 and 11) agreement between aerial-observed and modeled dye, here modeled and observed dye is compared at five in situ locations (indicated with FA-FD in Figure 9) within or along Topsail shoal between $-1000 < y < -210$ m (Figure 12). Similar to the inlet main channel location M (Figure 2c), model data dye agreement is good at location FA just downcoast of the main channel mouth (Figure 12a). The observed dye $D^{(obs)}$ increases rapidly shortly after the dye release starts and is relatively constant at 7 ppb until it rapidly returns to zero shortly after the dye release ends (blue in Figure 12a). At FA, the model dye $D^{(m)}$ is similar, with a longer ramp up and less variability (red in Figure 12a).

In contrast, the model data comparison is poor at location FB (Figure 9), within the small flood channel between the shoreline and Topsail shoal (Figure 12b). At FB, very little dye is observed except for a 1 h long burst that peaks at 5 ppb. In contrast, model dye ramps up shortly after dye release starts, is roughly constant near 10 ppb, and decays rapidly after the dye release ends. Along the Topsail shoal offshore 2 m depth contour at locations FC to FD (Figure 9), the dye arrival and departure timing is well modeled. However $D^{(m)}$ is 2× (FC) to 1.5× (FD) higher than observed (Figures 12c and 12d). This in situ model difference at FB, FC, and FD is consistent with the surface dye model data comparisons (Figures 3 and 4), particularly at FB, where flood channel model dye is too elevated. After $t = 18.0$ h as the inlet flood tide begins, weak $D^{(obs)}$ is observed at FA-FD (Figure 12) because a small portion of the dye returns to the inlet on flood. Model dye also returns to the inlet, but is even weaker, perhaps because $D^{(m)}$ is lost advecting out of the child-grid.

The last fixed location dye comparison is at the wirewalker at $(x, y) = (970, 7)$ m in $h = 8$ m that continuously sampled temperature, salinity, and dye from $z = -1.5$ m to $z = -6$ m below the surface. At the wirewalker, observed dye at 0.5–3 ppb was observed from $t = 14.0$ h to $t = 15.3$ h, in largely vertically uniform and intermittent bands (Figure 13a) suggesting an offshore weak meandering dye plume. The model dye is qualitatively similar in concentration, intermittency, and vertical uniformity (Figure 13b), although the specific timing is not captured. This suggests that the unstratified model with waves largely captures the small component of the dye plume that makes it into deeper water.

The model dye vertical uniformity is expected because the model is unstratified. Although observed temperature and salinity temporally evolved at the wirewalker, the largely depth-uniform observed dye results from the largely vertically uniform temperature and salinity (Figures 13c and 13d). At $t = 11.5$ h, just prior to ebb, the wirewalker temperature $T \approx 21.4\,^{\circ}$C and salinity $S \approx 35.5$ psu, both depth-uniform, indicative of "ocean" water. Over the course of the ebb-tidal flow (12.0–17.5 h), the temperature warms to $T \approx 23\,^{\circ}$C and freshens to $S \approx 35.2$ psu in a depth-uniform manner, as "inlet" water is transported past the wirewalker. Some warming also is expected from surface heating. In contrast to the dye spatial point source with 2.32 h release duration, "inlet" water has a source across the entire inlet with 6.5 h flood duration (Figure 2b). Thus, dye is not expected in all "inlet" water. Variability in T and S is present on 0.25–0.5 h time scales, consistent with the observed dye variability (Figure 13a), indicative of the ebb-tidal plume meandering. At the start of flood ($t = 18.0$ h), colder and saltier ocean water first intrude at the lower half of the water column, before occupying the entire water column by $t = 19.0$ h (Figures 13c and 13d). Wirewalker dye is not observed on the subsequent flood tide. The potential effect of lateral baroclinic pressure gradients induced by the "inlet" to "ocean" water variation are discussed in section 4.3.

4. Discussion

The qualitative (Figures 3–7) and statistical (Figures 8 and 11) dye model data comparison suggest that the model is capturing the main physical processes governing dye transport and dispersion between the inlet, inner shelf, and surfzone. Here the role of the bathymetry, wave forcing, and density variations in influencing dye tracer evolution are discussed.

4.1. The Role of Bathymetry in Modeled Dye Evolution

Although the 7 May model dye overall is similar to the observed, the model dye transport is overpredicted in the near-shoreline flood channel and across Topsail shoal (e.g., Figures 4 and 12). Model bathymetry errors are a prime culprit in this model discrepancy. Visual observations indicate that the portion of Topsail shoal bordering the main channel was very shallow during the dye release (see oval in Figure 14) and fully exposed at the lowest tide near $t = 15.0$ h, when boats could be beached on this shoal (J. Thomson, personal communication, 2012). This very shallow region potentially hindered observed dye from crossing Topsail shoal. The model bathymetry is based on an 10 May survey with $\Delta y = 50$ m alongshore resolution and is smoothed to remove high gradients that induce model pressure gradient errors [*Shchepetkin and McWilliams*, 2003]. In this shoal region, the model bathymetry always was wetted with shallowest depths $h + \eta$ of 0.5 and 0.3 m at $t = 13.33$ h and at (low tide) $t = 15.0$ h, respectively. Thus, the model bathymetry potentially was too deep in this region, allowing enhanced model dye transport across Topsail shoal. If the model did not bias the ebb-tidal elevation low (Figure 2a), the effect of the smoothed bathymetry would be more enhanced.

The smoothing of the model bathymetry likely has other effects on the model dye field. In the near field as observed dye crosses Topsail shoal, ≈ 50 m wide dye filaments are observed oriented almost in the $-y$ direction (Figure 3e), but are not present in the model (Figure 3f). These observed dye filaments are likely due to swash bars common on ebb-tidal deltas [e.g., *Hayes*, 1980]. Visual observations (e.g., Figure 14 and time-elapsed ARGUS video images, http://cil-www.coas.oregonstate.edu/) reveal gaps in breaking wave activity consistent with channels of swash bar troughs. These deeper regions presumably guide the ebb flow and induce the observed dye filaments (Figure 3e).

4.2. The Effect of Waves on Dye Transport

During the 7 May dye release, with relatively large and highly obliquely incident waves ($H_s = 1.2$ m, $\bar{\theta} = 34^{\circ}$), the observed dye plume turned (Figures 3 and 4) and propagated downcoast ($y < -1500$ m) in a narrow

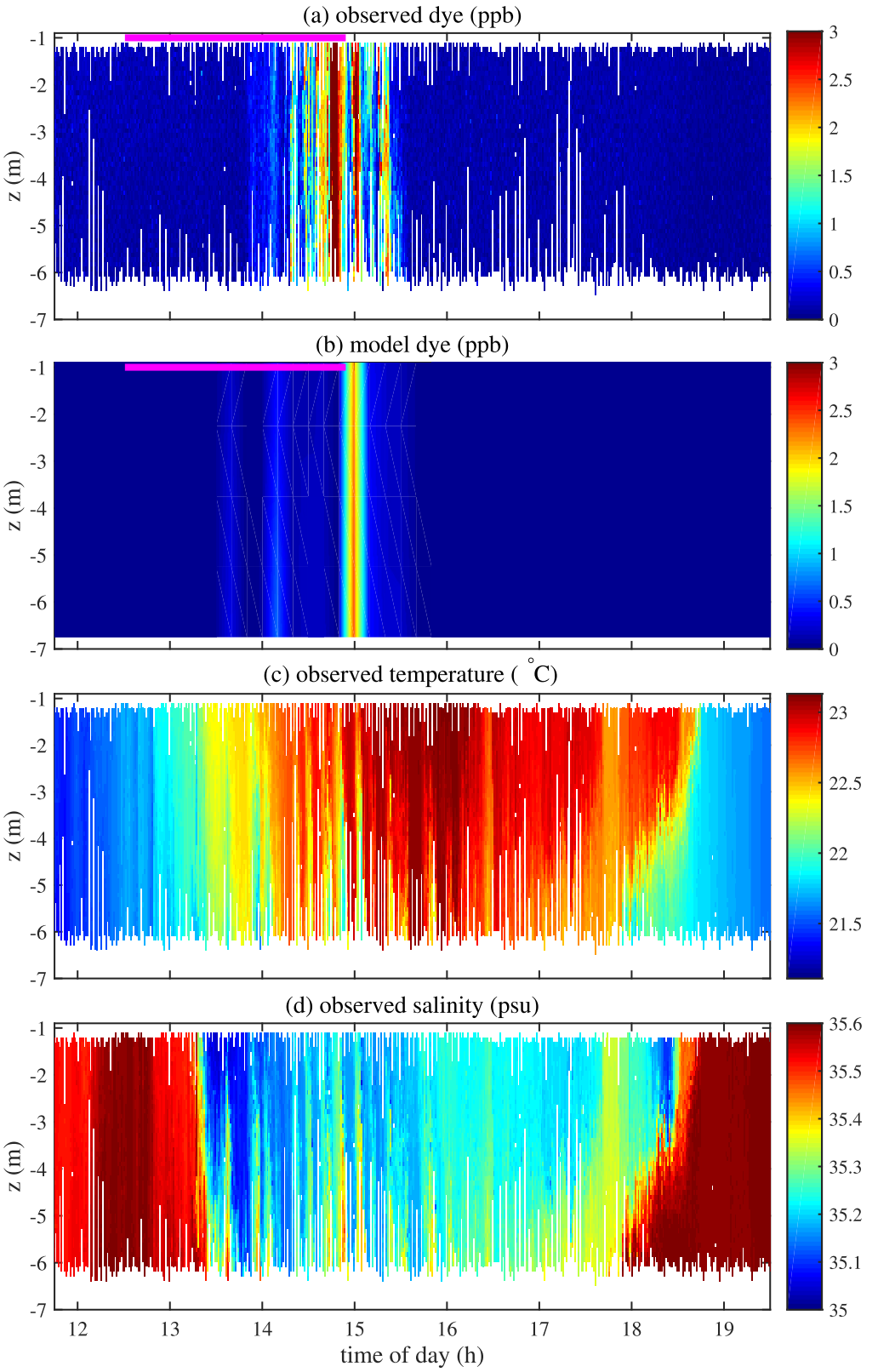

Figure 13. Wirewalker, located at $(x, y) = (970, 7)$ m, observations versus time and vertical z: (a) observed dye D, (b) model dye D, (c) observed temperature, and (d) observed salinity. In Figures 13a, 13c, and 13d, white are unsampled regions. Magenta bars in Figures 13a and 13b denote the dye release duration. Note that no dye was observed at the wirewalker to return to the inlet on the subsequent flood.

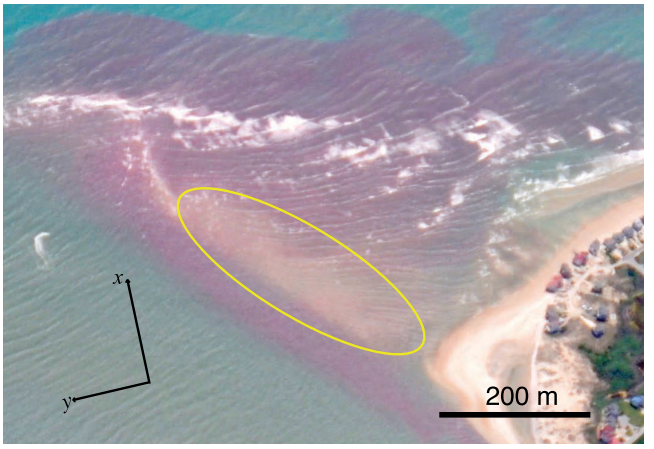

Figure 14. 7 May color-enhanced aerial photograph at $t = 13.33$ h of the Topsail Shoal looking out from within the inlet (see Figure 1) highlighting (yellow oval) the very shallow shoal (yellow oval) adjacent to the main channel where dye is transported offshore. The orientation of $(+x, +y)$ is indicated by the black arrows although note this is not the coordinate system origin. An approximate 200 m scale is given in the bottom right.

plume (Figures 6 and 7). The dye was not ejected offshore in a jet. Obliquely incident breaking waves are known to drive strong alongshore currents in the surfzone [e.g., *Longuet-Higgins*, 1970; *Thornton and Guza*, 1986; *Feddersen et al.*, 1998]. The effect of obliquely incident breaking waves on a tidal inlet ebb flow is less understood. Normally incident wave-breaking forcing retards offshore ebb-tidal jets in observations [*Orescanin et al.*, 2014] and models [*Olabarrieta et al.*, 2014]. Large waves can drive along-shoal flows, resulting in along-coast tracer transport [*Olabarrieta et al.*, 2014], suggesting that wave forcing, which increases with wave obliquity, may have a role in driving dye downcoast. Here the role of wave forcing in the dye evolution is explored with two additional 7 May simulations, one neglecting both wind and wave forcing (denoted NWW) and another neglecting only wave forcing (NW). Subsequently, the dynamical terms driving the flow are examined.

The NWW and NW simulations (Figure 15) have very different dye field evolution relative to the wind and wave (WWW) simulation (Figures 3–7). At $t = 15.0$ h, the NWW dye has one elongated lobe at 3 ppb ejected offshore to $x = 2000$ m, with an additional lobe at 15 ppb advecting over Topsail shoal and offshore across the 4 m depth contour (Figure 15a). No dye has advected downcoast and all dye is at $y > -1000$ m. The NW (with wind but no waves) simulated dye field has almost identical center of mass, but some dye has advected weakly to $y = 1200$ m due to wind forcing (Figure 15b). In stark contrast, the WWW simulation at $t = 15.0$ h (Figure 5d) has the leading edge of the dye plume at $y = -3500$ m and little dye is advected offshore.

Later at $t = 16.66$ h, the effect of wave forcing is even more dramatic (compare Figure 6b with Figures 15c and 15d). The NWW dye has not advected downcoast and is contained at $y > -1250$ m, in contrast to the WWW dye field. NWW dye has been transported farther offshore than WWW. One NWW lobe extends offshore beyond $x > 2500$ m and the second lobe is centered at $y = -900$ m on the 8 m contour. At $t = 16.66$ h, the NW (with wind, no waves) simulation does have dye moving downcoast due to wind (Figure 15d), but almost 3× more slowly than WWW. At $t = 16.66$ h, the dye mass fraction offshore of the 6 m depth contour (Figure 15) is 0.77 for NWW, 0.66 for NW, and only 0.33 for WWW (Figure 6b). These model results demonstrate the strong impact that waves have on the evolution of the dye plume.

With waves, dye is not ejected offshore in a jet. The classic ebb-tidal jet dynamical mix of horizontal advection, lateral mixing, and bottom stress ignores wave effects, which may be important at inlets similar to New River, with large obliquely incident waves propagating across complex bathymetry. Here WWW modeled depth-integrated momentum dynamical terms are used to diagnose the effects of waves and winds on the flow field transporting dye. Near the peak ebb-tidal flow ($t = 13.9$ h), model dye already has turned and advected downcoast to $y \approx -2000$ m (Figures 4f and 16a). Within the inlet main channel ($0 < x < 500$ m and $-400 < y < -100$ m), the combined pressure-gradient and nonlinear term (PG+NL, $-g(h+\eta)\nabla\eta - \nabla\cdot[(h+\eta)\mathbf{uu}]$) is directed offshore and largely balances the onshore-directed bottom stress term (Figures 16b and 16d). The tendency term ($\partial u/\partial t$) is small and the wave forcing term is negligible because waves are not breaking (Figure 16c). This is the expected dynamical balance [e.g., *Hench and Luettich*, 2003]. However, at the mouth of the main channel and along the offshore side of Topsail shoal, wave breaking (Figure 14) exerts a strong depth-integrated wave force (WF, $D_w\mathbf{k}/(|\mathbf{k}|c)$, where D_w is the wave dissipation, $\mathbf{k}$ is the wave number, and c is the phase speed). WF is oriented largely perpendicular to the local bathymetry contours, but also has a downcoast (–y) component (Figure 16c). This retards the outgoing jet and induces flow along the Topsail

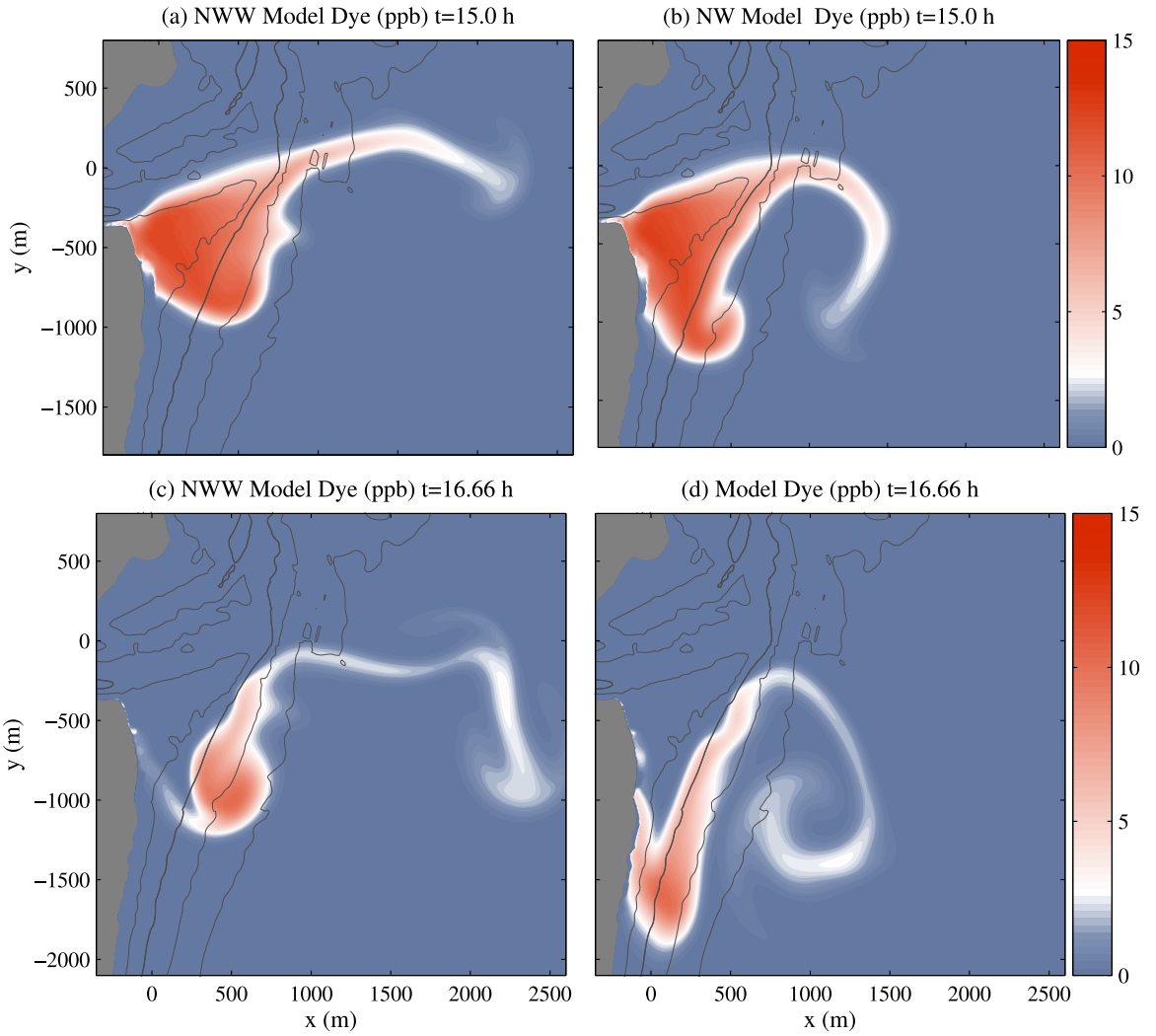

Figure 15. Modeled dye versus cross and alongshore coordinate at (top) $t = 15.0$ h and (bottom) $t = 16.6$ h for simulations with (a, c) no wave or wind forcing (NWW) and (b, d) no wave forcing (NW). Depth is contoured at 2, 4 (thick), 6, and 8 m.

shoal (as in *Olabarrieta et al.* [2014]), transporting dye downcoast (Figure 4). Everywhere in the inlet region, the Coriolis forcing term is 20× to 100× smaller than the PG, NL, or bottom stress terms.

To examine the alongshore momentum dynamics governing downcoast ($y < -2000$ m) tracer transport (Figures (6 and 7), and 17a), vector momentum terms are rotated into a downcoast coordinate system (x', y') with y' parallel to the coast (Figure 17c). In the downcoast region within 200 m of the shoreline, the dominant alongshore momentum balance is between wave forcing and bottom stress, with magnitudes around $10^{-3}\,m^2\,s^{-2}$ (Figures 17c and 17d). Alongshore pressure gradient and nonlinear terms (Figure 17b) are smaller, yet relevant and arise from bathymetric variations at 500 m scales. This largely traditional surfzone momentum balance [e.g., *Feddersen et al.*, 1998] drives the downcoast ($y < -2000$ m) transport of the ≈ 200 m wide model dye plume (Figure 17a). Given the model data similarity, wave forcing also presumably is driving the observed downcoast dye transport. Offshore of the surfzone, the alongcoast momentum balance is principally between bottom stress and wind stress at magnitudes of $5\times10^{-5}\,m^2\,s^{-2}$, much weaker than within the surfzone, with other terms (mostly PG and NL) weaker but also contributing. This is essentially a traditional wind-driven inner-shelf dynamical balance [e.g., *Lentz and Winant*, 1986; *Lentz et al.*, 1999; *Kumar et al.*, 2015].

On other days (17, 19, 20 May) at New River Inlet, a buoyant inlet plume propagated offshore [*Rogowski et al.*, 2014]. However, those days had smaller wave heights with $H_s = (0.75, 1.1, 0.82)$ m and less wave

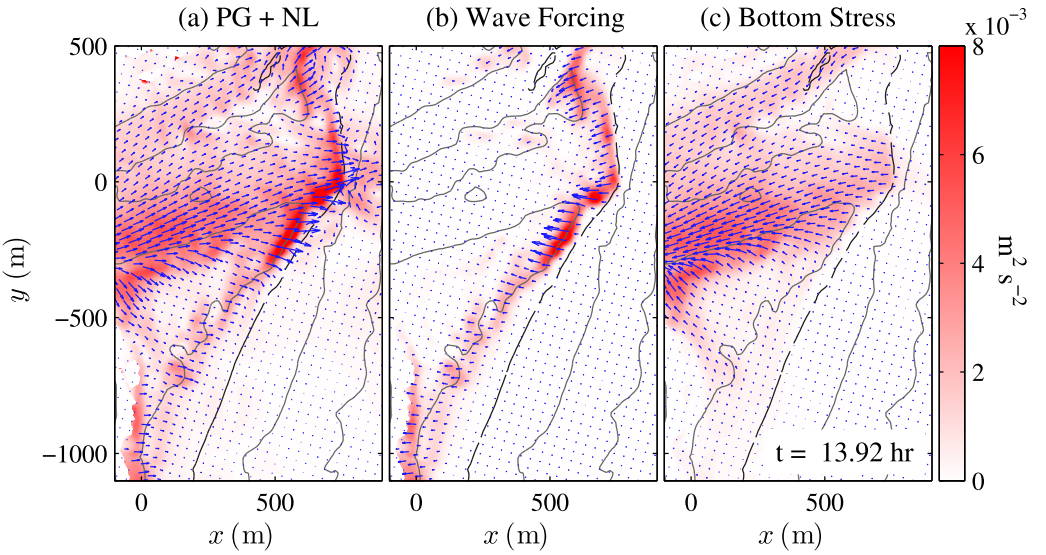

Figure 16. Inlet-mouth modeled depth-integrated momentum terms (a) pressure gradient plus nonlinear advection (PG+NL) (b) wave forcing and (c) bottom stress as a function of x and y at time t = 13.92 h. Depth is contoured at 2, 4 (thick), 6, and 8 m.

obliquity ($\bar{\theta}=[14°, 22°, 14°]$) than 7 May ($H_s$=1.2 m, $\bar{\theta}$=34°), reducing the alongshore wave forcing by 40–80%. In addition, these buoyant plumes had a source region across the entire inlet, and not just a spatial point source near Topsail beach (pink triangle in Figure 1). Coupled wave and circulation modeling suggests that a portion of the 19 May (H_s=1.1 m and $\langle\bar{\theta}\rangle$=22°) ebb-tidal jet was turned downcoast [*Rogowski et al.*, 2014], further reinforcing the importance of wave effects [e.g., *Olabarrieta et al.*, 2014].

4.3. Effect of Temperature and Density Variations

Many dye field features are modeled accurately with the constant density assumption. However, wirewalker and CTD cast observations show that the "ocean" and "inlet" water have different temperature and salinity.

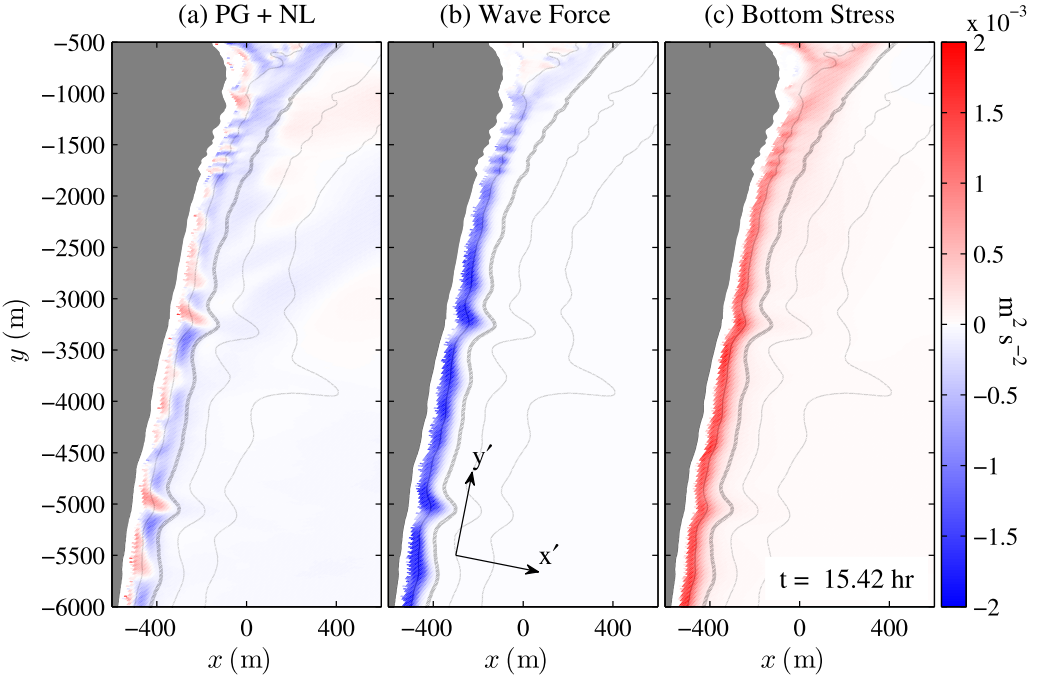

Figure 17. Downcoast region modeled depth-integrated alongshore (+y') momentum terms (a) pressure gradient (PG) plus nonlinear advection (NL) (b) wave forcing, and (c) bottom stress as a function of x and y at time t = 15.42 h. Depth is contoured at 2, 4 (thick), 6, and 8 m.

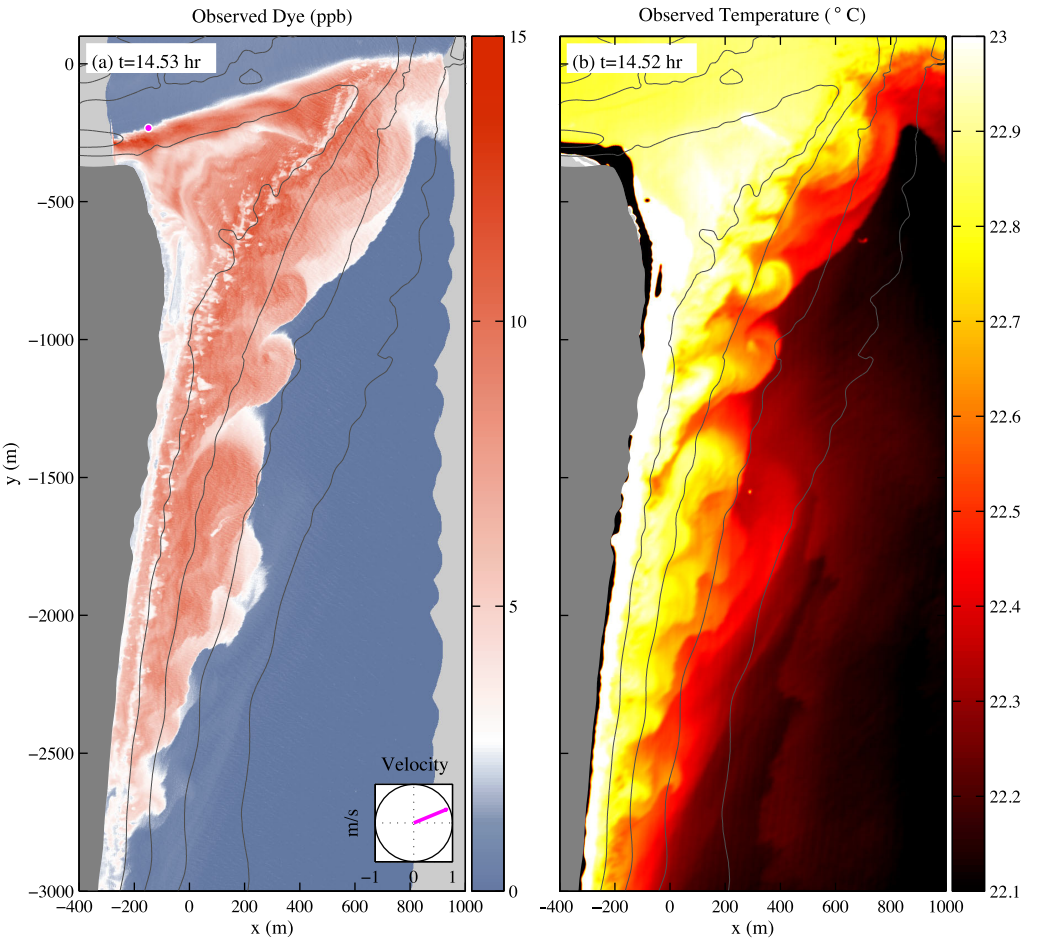

Figure 18. Midfield observed dye (left) and temperature (right) with bathymetry (2, 4, 6, and 8 m) contours as a function of cross-shore x and alongshore y coordinate for time $t \approx 14.53$ h near peak ebb flow (Figure 2b). Land is indicated with dark gray. In Figure 18a, light gray regions are outside aerial hyperspectral observations. In Figure 18b, small dark regions adjacent to the dark gray land mask are artifacts of mask inaccuracies.

Aerial-based surface dye and temperature observations (section 2.1.2) are now examined jointly, both in the role of temperature as a second passive tracer marking "inlet" and "ocean" water and in its potential dynamical role as gravity current.

As with dye, temperature also has an "inlet" source because the shallow waters within and up-inlet are heated more rapidly than deeper ocean waters. Thus, some covariation of dye and temperature is expected. In the later midfield ($t = 14.53$ h) when dye has been transported downcoast to $y \approx -3000$ m in the wave-driven surfzone and wind-driven inner-shelf plume, the dye and temperature field largely covary (Figure 18). In regions where $D \geq 5$ ppb, the surface $T \geq 22.7$ °C, reflecting "inlet" water. In offshore, dye-free regions, "ocean" water is cold ($T \leq 22.2$ °C). The boundary region between dye-free and dye-present water along the 2–6 m depth contour has a rich covarying thermal and dye structure. For example, cold water ($T \approx 22.5$ °C) intrusions onshore (to 2 m depth) into the dye plume region (e.g., $-1500 < y < -1100$ m) correspond to eddy-like dye features with reduced dye ≈ 3 ppb.

Less dense shoreline propagating plumes (in the northern hemisphere) are often associated with a gravity current with speed $(g\Delta\rho h_{\mathrm{dye}}/\rho_0)^{1/2}$ [e.g., *Rennie et al.*, 1999], where $\Delta\rho$ is the ocean to inlet density difference, $\rho_0 = 1024\,\mathrm{kg\,m^{-3}}$ is the background density, and $h_{\mathrm{dye}} = 3.5$ m is the layer thickness (Figure 10). The "inlet" to "ocean" temperature difference $\Delta T \approx 0.75$ °C and salinity difference $\Delta S \approx 0.2$ psu results in a $\Delta\rho = 0.37\,\mathrm{kg\,m^{-3}}$, far weaker than the $\Delta\rho$ of 2–3 $\mathrm{kg\,m^{-3}}$ in a buoyant coastal current observed 90 km south of Chesapeake Bay entrance [*Lentz et al.*, 2003]. The associated gravity current speed of $0.03\,\mathrm{m\,s^{-1}}$ is weaker than the observed $0.30\,\mathrm{m\,s^{-1}}$ downcoast transport rate, suggesting that for time scales (few hours) short

relative to the geostrophic adjustment time, "inlet" to "ocean" water density variations do not have a first-order dynamical effect. Far downstream and in depths >5 m, density variations do have some effect on the vertical structure of the dye field (e.g., cast B in Figure 10) by reducing vertical mixing. For calmer wave and wind conditions, the New River Inlet plume is more likely to advect offshore into deeper water, and density variations will become more important [*Rogowski et al*., 2014; *Spydell et al*., 2015].

5. Summary

A 9 km long tracer plume was created by continuously releasing Rhodamine WT dye for 2.2 h during ebb tide within the southern edge of the well-mixed main tidal channel at New River Inlet, NC. Observed (aerial hyperspectral and in situ) dye concentrations compare well with COAWST (coupled ROMS/SWAN) numerical simulations that include forcing by waves, wind, and tides. Dye was first transported seaward along the main channel, and advected to the offshore edge of the ebb-tidal shoal. The dye did not eject offshore in an ebb-tidal jet as previously observed at this site, because moderately energetic and highly oblique breaking wind waves retarded the inlet-mouth ebb-tidal flow, and forced currents along and across the ebb shoal. Consequently, the dye plume was trapped on the ebb-tidal shoal, after which it was transported downcoast at 0.3 m s^{-1} in the narrow (few 100 m wide) surfzone driven by wave breaking. Modeled dye is qualitatively similar to the observed. Observed and modeled surface dye moments are in agreement. The observed dye mass balances close, indicating all released dye is accounted for. Regional ("inlet" and "ocean") observed and modeled dye mass balances also agree, but details of dye transport pathways are modeled poorly likely owing to inaccurate (oversmoothed) model bathymetry. Although temperature acts as a second tracer of inlet water, the dye plume is not significantly affected by buoyancy. Wave forcing effects have a large impact on the dye transport.

Acknowledgments

This research was supported by the Littoral Geosciences and Optics Division of the Office of Naval Research as part of the Tidal Inlets and River Mouths Directed Research Initiative. Staff, students, and volunteers from SIO (B. Woodward, B. Boyd, K. Smith, D. Darnell, Z. Dagan, M. M. Omand, B. Ludka, A. Doria, K. Hally-Rosendahl, and J. Wanetick) and the PVLAB at WHOI were instrumental in acquiring the field observations. In addition, colleagues at the Naval Postgraduate School (Jamie MacMahan, Jenna Brown, and Micah Weltmer), Delft University (Ad Reniers), and University of Miami (Patrick Rynne) provided valuable support. The University of Washington Applied Physics Lab (Jim Thomson and Chris Chickadel) and Eric Terrill provided wind observations. Luc Lenain and Nick Statom from the SIO air-sea interaction laboratory led by W. K. Melville acquired the aerial hyperspectral and infrared data with the MASS system. The US Army Corp of Engineers Field Research Facility provided high-quality bathymetry surveys. We thank these people and organizations. Data are available from https://scripps.ucsd.edu/projects/RIV-ET/and from the authors.

References

Bertin, X., A. B. Fortunato, and A. Oliveira (2009), A modeling-based analysis of processes driving wave-dominated inlets, *Cont. Shelf Res.*, *29*(5–6), 819–834, doi:10.1016/j.csr.2008.12.019.

Booij, N., R. C. Ris, and L. H. Holthuijsen (1999), A third-generation wave model for coastal regions, Part I, Model description and validation, *J. Geophys. Res.*, *104*(C4), 7647–7666, doi:10.1029/98JC02622.

Chadwick, D. B., and J. L. Largier (1999), Tidal exchange at the bay-ocean boundary, *J. Geophys. Res.*, *104*(C12), 29,901–29,924, doi:10.1029/1999JC900165.

Chant, R. J., W. R. Geyer, R. Houghton, E. Hunter, and J. Lerczak (2007), Estuarine boundary layer mixing processes: Insights from dye experiments, *J. Phys. Oceanogr.*, *37*, 1859–1877, doi:10.1175/JPO3088.1.

Chassignet, E. P., et al. (2000), DAMEE-NAB: The base experiments, *Dyn. Atmos. Oceans*, *32*, 155–183, doi:10.1016/S0377-0265(00)00046-4.

Chen, F., D. G. MacDonald, and R. D. Hetland (2009), Lateral spreading of a near-field river plume: Observations and numerical simulations, *J. Geophys. Res.*, *114*, C07013, doi:10.1029/2008JC004893.

Chen, J. L., F. Hsu, T. J. Shi, B. Raubenheimer, and S. Elgar (2015), Hydrodynamic and sediment transport modeling of New River Inlet (NC) under the interaction of tides and waves, *J. Geophys. Res. Oceans*, *120*, 4028–4047, doi:10.1002/2014JC010425.

Clark, D. B., F. Feddersen, M. M. Omand, and R. T. Guza (2009), Measuring fluorescent dye in the bubbly and sediment laden surfzone, *Water Air Soil Poll.*, doi:10.1007/s11270-009-0030-z.

Clark, D. B., F. Feddersen, and R. T. Guza (2010), Cross-shore surfzone tracer dispersion in an alongshore current, *J. Geophys. Res.*, *115*, C10035, doi:10.1029/2009JC005683.

Clark, D. B., L. Lenain, F. Feddersen, E. Boss, and R. T. Guza (2014), Aerial imaging of fluorescent dye in the nearshore, *J. Atmos. Oceanic Technol.*, *31*, 1410–1421, doi:10.1175/JTECH-D-13-00230.1.

Delpey, M. T., F. Ardhuin, P. Otheguy, and A. Jouon (2014), Effects of waves on coastal water dispersion in a small estuarine bay, *J. Geophys. Res. Oceans*, *119*, 70–86, doi:10.1002/2013JC009466.

de Swart, H., and J. Zimmerman (2009), Morphodynamics of tidal inlet systems, *Annu. Rev. Fluid Mech.*, *41*(1), 203–229, doi:10.1146/annurev.fluid.010908.165159.

Dodet, G., X. Bertin, N. Bruneau, A. B. Fortunato, A. Nahon, and A. Roland (2013), Wave-current interactions in a wave-dominated tidal inlet, *J. Geophys. Res. Oceans*, *118*, 1587–1605, doi:10.1002/jgrc.20146.

Elias, E. P. L., G. Gelfenbaum, and A. J. Van der Westhuysen (2012), Validation of a coupled wave-flow model in a high-energy setting: The mouth of the Columbia river, *J. Geophys. Res.*, *117*, C09011, doi:10.1029/2012JC008105.

Feddersen, F., R. T. Guza, S. Elgar, and T. H. C. Herbers (1998), Alongshore momentum balances in the nearshore, *J. Geophys. Res.*, *103*(C8), 15,667–15,676.

Fong, D. A., and W. R. Geyer (2001), Response of a river plume during an upwelling favorable wind event, *J. Geophys. Res.*, *106*(C1), 1067–1084, doi:10.1029/2000JC900134.

Garvine, R. W. (1982), A steady state model for buoyant surface plume hydrodynamics in coastal waters, *Tellus*, *34*(3), 293–306, doi:10.1111/j.2153-3490.1982.tb01818.x.

Garvine, R. W. (1984), Radial spreading of buoyant, surface plumes in coastal waters, *J. Geophys. Res.*, *89*(C2), 1989–1996, doi:10.1029/JC089iC02p01989.

Garvine, R. W. (1999), Penetration of buoyant coastal discharge onto the continental shelf: A numerical model experiment, *J. Phys. Oceanogr.*, *29*, 1892–1909, doi:10.1175/1520-0485(1999)029<1892:POBCDO>2.0.CO;2.

Gerbi, G. P., S. E. Kastner, and G. Brett (2015), The role of whitecapping in thickening the ocean surface boundary layer, *J. Phys. Oceanogr.*, *45*, 2006–2024, doi:10.1175/JPO-D-14-0234.1.
Geyer, W. R., and P. MacCready (2014), The estuarine circulation, *Annu. Rev. Fluid Mech.*, *46*(1), 175–197, doi:10.1146/annurev-fluid-010313-141302.
Haidvogel, D. B., H. G. Arango, K. Hedstrom, A. Beckmann, P. Malanotte-Rizzoli, and A. F. Shchepetkin (2000), Model evaluation experiments in the North Atlantic Basin: Simulations in nonlinear terrain-following coordinates, *Dyn. Atmos. Oceans*, *32*, 239–281, doi:10.1016/S0377-0265(00)00049-X.
Haidvogel, D. B., et al. (2008), Regional ocean forecasting in terrain-following coordinates: Model formulation and skill assessment, *J. Comput. Phys.*, *227*(7), 3595–3624, doi:10.1016/j.jcp.2007.06.016.
Hally-Rosendahl, K., F. Feddersen, D. B. Clark, and R. T. Guza (2015), Surfzone to inner-shelf exchange estimated from dye tracer balances, *J. Geophys. Res. Oceans*, *120*, 6289–6308, doi:10.1002/2015JC010844.
Hayes, M. O. (1980), General morphology and sediment patterns in tidal inlets, *Sediment. Geol.*, *26*(1), 139–156, doi:10.1016/0037-0738(80)90009-3.
Hayes, M. O., and D. M. FitzGerald (2013), Origin, evolution, and classification of tidal inlets, *J. Coastal Res.*, *69*, pp. 14–33, doi:10.2112/SI_69_3.
Hench, J. L., and R. A. Luettich (2003), Transient tidal circulation and momentum balances at a shallow inlet, *J. Phys. Oceanogr.*, *33*, 913–932, doi:10.1175/1520-0485(2003)33 < 913:TTCAMB>2.0.CO;2.
Horner-Devine, A. R., R. D. Hetland, and D. G. MacDonald (2015), Mixing and transport in coastal river plumes, *Annu. Rev. Fluid Mech.*, *47*(1), 569–594, doi:10.1146/annurev-fluid-010313-141408.
Ismail, N. M., and R. L. Wiegel (1983), Opposing wave effect on momentum jets spreading rate, *J. Waterw. Port Coastal Ocean Eng.*, *109*(4), 465–483, doi:10.1061/(ASCE)0733-950X(1983)109:4(465).
Joshi, P. B. (1982), Hydromechanics of tidal jets, *J. Waterw. Port Coastal Ocean Div.*, *108*(3), 239–253.
Kumar, N., G. Voulgaris, J. C. Warner, and M. Olabarrieta (2012), Implementation of the vortex force formalism in the coupled ocean-atmosphere-wave-sediment transport (COAWST) modeling system for inner shelf and surf zone applications, *Ocean Modell.*, *47*, 65–95, doi:10.1016/j.ocemod.2012.01.003.
Kumar, N., F. Feddersen, Y. Uchiyama, J. McWilliams, and W. O'Reilly (2015), Mid-shelf to surf zone coupled ROMS-SWAN model-data comparison of waves, currents, and temperature: Diagnosis of subtidal forcings and response, *J. Phys. Oceanogr.*, *45*, 1464–1490, doi:10.1175/JPO-D-14-0151.1.
Lentz, S., and C. Winant (1986), Subinertial currents on the southern California Shelf, *J. Phys. Oceanogr.*, *16*(11), 1737–1750.
Lentz, S., R. T. Guza, S. Elgar, F. Feddersen, and T. H. C. Herbers (1999), Momentum balances on the North Carolina inner shelf, *J. Geophys. Res.*, *104*(C8), 18,205–18,240, doi:10.1029/1999JC900101.
Lentz, S. J., S. Elgar, and R. T. Guza (2003), Observations of the flow field near the nose of a buoyant coastal current, *J. Phys. Oceanogr.*, *33*(4), 933–943, doi:10.1175/1520-0485(2003)33¡933:OOTFFN¿2.0.CO;2.
Longuet-Higgins, M., and R. Stewart (1964), Radiation stresses in water waves—A physical discussion, with applications, *Deep Sea Res. Oceanogr. Abstr.*, *11*(4), 529–562, doi:10.1016/0011-7471(64)90001-4.
Longuet-Higgins, M. S. (1970), Longshore currents generated by obliquely incident sea waves: 1, *J. Geophys. Res.*, *75*(33), 6778–6801.
MacCready, P., and W. R. Geyer (2010), Advances in estuarine physics, *Annu. Rev. Mar. Sci.*, *2*(1), 35–58, doi:10.1146/annurev-marine-120308-081015.
MacMahan, J., J. van de Kreeke, A. Reniers, S. Elgar, B. Raubenheimer, E. Thornton, M. Weltmer, P. Rynne, and J. Brown (2014), Fortnightly tides and subtidal motions in a choked inlet, *Estuarine Coastal Shelf Sci.*, *150*, 325–331, doi:10.1016/j.ecss.2014.03.025.
McCabe, R. M., P. MacCready, and B. M. Hickey (2009), Ebb-tide dynamics and spreading of a Large River Plume, *J. Phys. Oceanogr.*, *39*, 2839–2856, doi:10.1175/2009JPO4061.1.
McWilliams, J. C., J. M. Restrepo, and E. M. Lane (2004), An asymptotic theory for interaction of waves and currents in coastal waters, *J. Fluid Mech.*, *511*, 135–178, doi:10.1017/S0022112004009358.
Mehta, A. J., and P. B. Joshi (1988), Tidal inlet hydraulics, *J. Hydraul. Eng.*, *114*(11), 1321–1338, doi:10.1061/(ASCE)0733-9429(1988)114:11(1321).
Melville, W. K., L. Lenain, D. R. Cayan, M. Kahru, J. P. Kleissl, P. F. Linden, and N. M. Statom (2016), The modular aerial sensing system, *J. Atmos. Oceanic Technol.*, *33*(6), 1169–1184, doi:10.1175/JTECH-D-15-0067.1.
Olabarrieta, M., J. C. Warner, and N. Kumar (2011), Wave-current interaction in Willapa Bay, *J. Geophys. Res.*, *116*, C12014, doi:10.1029/2011JC007387.
Olabarrieta, M., R. Geyer, and N. Kumar (2014), The role of morphology and wave-current interaction at tidal inlets: An idealized modeling analysis, *J. Geophys. Res.*, *119*, 8818–8837, doi:10.1002/2014JC010191.
Orescanin, M., B. Raubenheimer, and S. Elgar (2014), Observations of wave effects on inlet circulation, *Cont. Shelf Res.*, *82*, 37–42, doi:10.1016/j.csr.2014.04.010.
Ozsoy, E., and U. Unluata (1982), Ebb-tidal flow characteristics near inlets, *Estuarine Coastal Shelf Sci.*, *14*(3), 251−263.
Rennie, S. E., J. L. Largier, and S. J. Lentz (1999), Observations of a pulsed buoyancy current downstream of Chesapeake Bay, *J. Geophys. Res.*, *104*(C8), 18,227–18,240, doi:10.1029/1999JC900153.
Rogowski, P., E. Terrill, and J. Chen (2014), Observations of the frontal region of a buoyant river plume using an autonomous underwater vehicle, *J. Geophys. Res. Oceans*, *119*, 7549–7567, doi:10.1002/2014JC010392.
Shchepetkin, A. F., and J. C. McWilliams (2003), A method for computing horizontal pressure-gradient force in an oceanic model with a nonaligned vertical coordinate, *J. Geophys. Res.*, *108*(C3), 3090, doi:10.1029/2001JC001047.
Shchepetkin, A. F., and J. C. McWilliams (2005), The regional oceanic modeling system (ROMS): A split-explicit, free-surface, topography-following-coordinate oceanic model, *Ocean Modell.*, *9*(4), 347–404, doi:10.1016/j.ocemod.2004.08.002.
Smart, P. L., and I. M. S. Laidlaw (1977), An evaluation of some fluorescent dyes for water tracing, *Water Resour. Res.*, *13*(1), 15–33.
Spydell, M. S., F. Feddersen, M. Olabarrieta, J. Chen, R. T. Guza, B. Raubenheimer, and S. Elgar (2015), Observed and modeled drifters at a tidal inlet, *J. Geophys. Res. Oceans*, *120*, 4825–4844, doi:10.1002/2014JC010541.
Taylor, G. (1953), Dispersion of soluble matter in solvent flowing slowly through a tube, *Proc. Roy. Soc. A*, *219*, 186–203, doi:10.1098/rspa.1953.0139.
Tennekes, H., and J. L. Lumley (1972), *A First Course in Turbulence*, MIT Press, Cambridge, Mass.
Thomson, J., A. R. Horner-Devine, S. Zippel, C. Rusch, and W. Geyer (2014), Wave breaking turbulence at the offshore front of the Columbia river plume, *Geophys. Res. Lett.*, *41*, 8987–8993, doi:10.1002/2014GL062274.

Thornton, E. B., and R. T. Guza (1986), Surf zone longshore currents and random waves: Field data and models, *J. Phys. Oceanogr.*, *16*(7), 1165–1178.

Tulloch, R., et al. (2014), Direct estimate of lateral eddy diffusivity upstream of Drake passage, *J. Phys. Oceanogr.*, *44*, 2593–2616, doi: 10.1175/JPO3088.1.

Uchiyama, Y., J. C. McWilliams, and A. F. Shchepetkin (2010), Wave-current interaction in an oceanic circulation model with a vortex-force formalism: Application to the surf zone, *Ocean Modell.*, *34*(1–2), 16–35, doi:10.1016/j.ocemod.2010.04.002.

Wargula, A., B. Raubenheimer, and S. Elgar (2014), Wave-driven along-channel subtidal flows in a well-mixed ocean inlet, *J. Geophys. Res. Oceans*, *119*, 2987–3001, doi:10.1002/2014JC009839.

Warner, J. C., B. Armstrong, R. He, and J. B. Zambon (2010), Development of a coupled ocean-atmosphere-wave-sediment transport (COAWST) modeling system, *Ocean Modell.*, *35*, 230–244, doi:10.1016/j.ocemod.2010.07.010.

Wolanski, E., and J. Imberger (1987), Friction-controlled selective withdrawal near inlets, *Estuarine Coastal Shelf Sci.*, *24*(3), 327–333, doi: 10.1016/0272-7714(87)90053-9.

Zippel, S., and J. Thomson (2015), Wave breaking and turbulence at a tidal inlet, *J. Geophys. Res. Oceans*, *120*, 1016–1031, doi:10.1002/ 2014JC010025.